

Lunar swirls: Examining crustal magnetic anomalies and space weathering trends

David T. Blewett,¹ Ecaterina I. Coman,^{1,2} B. Ray Hawke,³ Jeffrey J. Gillis-Davis,³ Michael E. Purucker,⁴ and Christopher G. Hughes⁵

Received 19 May 2010; revised 29 September 2010; accepted 12 October 2010; published 3 February 2011.

[1] We have used multispectral images from Clementine and data from Lunar Prospector's magnetometer to conduct a survey of lunar crustal magnetic anomalies, prominent lunar swirls, and lesser known swirl markings to provide new information on the nature of swirls and their association with magnetic anomalies. We find that all swirls and swirl-like albedo patterns are associated with areas of magnetized crust, but not all areas of magnetized crust are colocated with swirl-like albedo anomalies. All observed swirls exhibit spectral characteristics similar to immature material and generally have slightly lower FeO values compared with their surroundings as determined with a multispectral iron-mapping method. We discuss these results in relation to the various hypotheses for swirl formation. The comet impact hypothesis for lunar swirls would not predict a difference in the spectrally determined FeO content between swirls and nearby ordinary surfaces. The compositional difference could be explained as a consequence of (1) magnetic shielding of the surface from the solar wind, which could produce anomalous space weathering (little darkening with limited reddening) and potentially alter the predictions of the multispectral iron-mapping algorithm while the compositional contrast could be enhanced by delivery of lower-FeO ejecta from outside the swirl; and (2) accumulation of fine plagioclase-rich dust moving under the influence of electric fields induced by solar wind interactions with a magnetic anomaly. Therefore, we cannot at present clearly distinguish between the solar wind shielding and electrostatic dust accumulation models for swirl formation. We describe future measurements that could contribute to solution of the puzzle of swirl origin.

Citation: Blewett, D. T., E. I. Coman, B. R. Hawke, J. J. Gillis-Davis, M. E. Purucker, and C. G. Hughes (2011), Lunar swirls: Examining crustal magnetic anomalies and space weathering trends, *J. Geophys. Res.*, 116, E02002, doi:10.1029/2010JE003656.

1. Introduction

[2] The particles and fields subsatellites carried aboard Apollo 15 and 16 revealed the presence of areas of magnetized crust on the Moon [e.g., *Coleman et al.*, 1972; *Russell et al.*, 1975; *Hood et al.*, 1981]. The inclination of the satellite orbits limited mapping of the surface fields to equatorial and midlatitudes. Global coverage was provided by the polar-orbiting Lunar Prospector spacecraft's magnetometer [*Hood et al.*, 2001] and electron reflectometer [*Halekas et al.*, 2001]. The Lunar Prospector data confirmed

the presence of magnetic anomalies mapped with Apollo data, such as those at Reiner Gamma and Rima Sirsalis, and also led to the discovery of a number of additional magnetic anomalies. A key question concerning these crustal frozen fields relates to the source of the original magnetizing field [e.g., *Hood*, 1995; *Richmond and Hood*, 2008a, 2008b]. The magnetization could have resulted from an ancient core dynamo [e.g., *Garrick-Bethell et al.*, 2009b; *Wieczorek and Weiss*, 2010; *Hood*, 2010], or by transient fields produced via amplification of ambient fields during basin-forming impacts [*Hood and Vickery*, 1984; *Hood and Huang*, 1991; *Crawford and Schultz*, 1999; *Hood and Artemieva*, 2008]. The observation that many, though not all, magnetic anomalies are found antipodal to major impact basins [*Lin et al.*, 1988; *Hood et al.*, 2001; *Richmond et al.*, 2005; *Mitchell et al.*, 2008] supports the idea that the formation of the magnetic anomalies relates to the formation of the basins. Another impact-related hypothesis concerns remnant magnetism impressed on the surface during the relatively recent collision of a cometary coma with the Moon [*Schultz and Srnka*, 1980].

[3] Lunar crustal magnetic anomalies are also of interest because of their link to the class of enigmatic high-albedo

¹Johns Hopkins University Applied Physics Laboratory, Laurel, Maryland, USA.

²University of Maryland-Baltimore County, Baltimore, Maryland, USA.

³Hawaii Institute of Geophysics and Planetology, University of Hawaii, Honolulu, Hawaii, USA.

⁴Raytheon at Planetary Geodynamics Laboratory, NASA Goddard Space Flight Center, Greenbelt, Maryland, USA.

⁵Department of Geology and Planetary Science, University of Pittsburgh, Pittsburgh, Pennsylvania, USA.

markings known as lunar swirls [e.g., *El-Baz*, 1972; *Hood et al.*, 1979a, 1979b, 2001; *Hood and Williams*, 1989; *Richmond et al.*, 2005]. Many of the prominent swirls, such as the Reiner Gamma Formation and the swirls in Mare Ingenii and Mare Marginis, among others, are colocated with magnetic anomalies. The classic swirls, exemplified by the Reiner Gamma Formation, consist of high-reflectance ribbons and loops that can stretch for several hundred kilometers across the lunar surface, with “dark lanes” sometimes enclosed within the sinuous bright markings. The swirls lack perceptible topography at the resolution of currently available images.

[4] Recently, a continuum of swirl morphologies has been recognized with the complex Reiner Gamma-type pattern as one end-member [*Blewett et al.*, 2007b]. At the other extreme is an anomalous diffuse bright spot, such as the one found in the Descartes highlands (discussed below in section 4.1). Intermediate forms consist of a simpler bright loop with a dark lane. An example of this type is located near Airy crater (section 4.2 below). The complex variety of swirl is more common in mare locations, while highland swirls are more likely to be less well developed [*Blewett et al.*, 2007b].

[5] The leading hypotheses that have been advanced for the formation of the swirls are (1) regolith disturbance caused by the relatively recent impact of a comet coma, cometary fragments, or cometary meteor swarms [*Schultz and Srnka*, 1980; *Pinet et al.*, 2000; *Starukhina and Shkuratov*, 2004]; (2) atypical space weathering as a result of the magnetic anomaly shielding the surface from solar wind ion bombardment [*Hood and Schubert*, 1980; *Hood and Williams*, 1989]; and (3) preferential accumulation of fine, feldspar-rich dust caused by attraction and repulsion of levitated dust grains by electric fields induced by solar wind interaction with the magnetic anomaly [*Garrick-Bethell et al.*, 2009a, 2010].

[6] The origin of the lunar swirls is an outstanding puzzle in lunar geoscience. In addition, the swirls lie at the intersection of broader issues in planetary science, including planetary magnetism and the agent of space weathering. There has been controversy concerning the relative importance of solar wind sputtering and implantation versus micrometeoroid bombardment in producing the optical effects of space weathering [e.g., *Pieters et al.*, 2000; *Hapke*, 2001]. The lunar swirls are thus important natural laboratories for understanding space weathering processes, which affect the interpretation of remote-sensing observations of airless rocky solar system bodies such as Mercury and the asteroids in addition to the Moon.

[7] In this contribution, we have examined the better known swirls, several lesser known swirl markings, and newly discovered magnetic anomalies in order to provide new information on the nature of swirls and their association with magnetic anomalies. The goals of the study are to (1) determine if unusual albedo markings are associated with recently identified magnetic anomalies; (2) determine if magnetic anomalies are present at several previously known but little-studied swirl occurrences; (3) evaluate differences in swirl morphology between highland and mare locations; (4) analyze spectral reflectance trends related to regolith composition and maturity in high-albedo swirl areas and make comparisons with trends in the surrounding surfaces; and

(5) examine the implications of our findings for the various hypotheses of swirl formation.

2. Data

[8] Our primary image data were obtained by the Clementine ultraviolet/visible (UV-Vis) camera. Clementine image cubes (200 m/pixel in five wavelengths: 415, 750, 900, 950, and 1000 nm) used for morphological and spectral analysis are calibrated to reflectance [*Eliason et al.*, 1999; *Isbell et al.*, 1999] and were obtained from the U.S. Geological Survey’s Map-A-Planet Web site (<http://www.mapaplanet.org/>). We present composites of three Clementine bands as pseudo-true color images. We have also used the Clementine images to produce ferrous iron (FeO) abundance and optical maturity maps [*Lucey et al.*, 2000a, 2000b]. The Clementine data were augmented by additional orbital photography from other sources, including Lunar Orbiter and Apollo.

[9] Information on the shapes and locations of crustal magnetic anomalies was obtained from maps of total field strength derived from Lunar Prospector magnetometer measurements, including those presented by *Hood et al.* [2001], *Richmond et al.* [2003, 2005], *Richmond and Hood* [2008a], *Purucker* [2008], and *Hood* [2010]. In addition, individual orbit passes were examined (L. L. Hood, personal communication, 2010) to further constrain the locations of the anomalies and to estimate their strengths at 30 km altitude. We have categorized the magnetic anomalies as weak, moderate, or strong based on their estimated peak strengths at 30 km altitude. The swirls and magnetic anomalies we studied are listed in Table 1.

3. Better Known Swirls

[10] This section focuses on the lunar swirl occurrences that are the most prominent in terms of visibility and that have received the most attention in the literature.

3.1. Reiner Gamma Formation

[11] The Reiner Gamma Formation in western Oceanus Procellarum is the type occurrence of a lunar swirl [*McCauley*, 1967]. It has been the subject of considerable interest [e.g., *El-Baz*, 1972; *Schultz and Srnka*, 1980; *Hood and Schubert*, 1980; *Bell and Hawke*, 1981, 1987; *Hood and Williams*, 1989; *Pinet et al.* 2000; *Starukhina and Shkuratov*, 2004; *Shkuratov et al.*, 2008]. Reiner Gamma is the only example of the full classic swirl morphology (extensive looping, sinuous, high-albedo ribbons with accompanying dark lanes) on the nearside of the Moon.

[12] We do not discuss Reiner Gamma extensively in this section, but present a Clementine mosaic (Figure 1) so that this important example can be compared with the other swirls illustrated in this paper. Several maps of the magnetic field strength over Reiner Gamma have been published, including those of *Hood* [1980], *Hood and Schubert* [1980], and *Hood et al.* [2001]. These maps show the peak of the magnetic anomaly to be centered on the brightest portion of the main swirl. Through examination of these maps, the global map of *Purucker* [2008] and individual Lunar Prospector orbit tracks from July 1999, the maximum of the field strength at 30 km altitude (assuming the strength falls as the -2 power of altitude) is estimated to be 22 nT (Table 1).

Table 1. Lunar Magnetic Anomalies Examined in this Study

Location	Approximate Lat., Long.	Setting	Magnetic Anomaly Strength, nT ^a	Swirl Character
Abel	30°S, 90°E	Mare/highland	10 – moderate	None recognized
Airy	18°S, 3.25°E	Highland	13 – moderate	Loop/dark lane
Crozier	15°S, 51°E	Mare/highland	6 – weak	None recognized
Descartes	15°S, 52°E	Highland	24 – strong	Diffuse bright spot
Firsov	10.5°S, 16.5°E	Highland	11 – moderate	Complex
Gerasimovich	21°S, 236.5°E	Highland	28 – strong	Loop/dark lane
Hartwig	10°S, 280°E	Highland/mare	12 – moderate	None recognized
Hopmann	48.5°S, 160°E	Mare/highland	5 – weak	Complex+loop
Ingenii	33.5°S, 160°E	Mare/highland	20 – strong	Complex
Marginis	16°N, 88°E	Mare/highland	6 – weak ^b	Complex
Moscoviense	27°N, 145°E	Mare	4 – weak	Complex
NW of Apollo	25°S, 197.5°E	Highland	12 – moderate	Loop/dark lane
Reiner Gamma	7.5°N, 302.5°E	Mare	22 – strong	Complex
Rima Sirsalis	8.5°S, 304.5°E	Mare/highland	8 – moderate	Loop/dark lane
Stöfler	40°S, 5°E	Highland	10 – moderate	None recognized

^aEstimated peak total field strength of magnetic anomaly at 30-km altitude: Weak, <7; moderate, 7–15; strong >15.

^bPoor coverage by Lunar Prospector magnetometer.

Further analysis of the spectral properties of the Reiner Gamma swirl is given in section 7.3.

3.2. Mare Ingenii

[13] Lunar Orbiter images provided good coverage of the prominent swirls found on Mare Ingenii, and these swirls are shown on the maps of *Stuart-Alexander* [1978], *Schultz and Srnka* [1980], and *Hood and Williams* [1989]. The complex, sinuous, high-albedo markings overlie the late-Imbrium mare basalts [*Stuart-Alexander*, 1978] and also appear to cross the highland units on the western shores of Mare Ingenii and the southwest rim of the Thomson crater (Figure 2). The area of the swirls is antipodal to the Imbrium basin, and highland units around Mare Ingenii include “grooved and mounded” material [*Stuart-Alexander*, 1978]. The unusual texture may be related to the formation of the Imbrium basin through antipodal coalescence of ejecta [*Moore et al.*, 1974; *Wieczorek and Zuber*, 2001] or seismic focusing [*Schultz and Gault*, 1975].

[14] The magnetic field structure over Mare Ingenii is delineated in Lunar Prospector maps for this area presented by *Hood et al.* [2001], *Richmond et al.* [2005], and *Richmond and Hood* [2008a]. The maximum of the field strength at 30 km altitude is estimated to be 20 nT, a value slightly less than that of the Reiner Gamma anomaly. The peak magnetic intensity is spatially coincident with the largest and highest reflectance portion of the swirl, over the southern section of Mare Ingenii and crater Thomson M. *Kramer et al.* [2010] have examined the spectra of small fresh craters in and near the Mare Ingenii swirls in order to evaluate the correlation between magnetic shielding and optical maturation.

3.3. Mare Marginis

[15] Swirls on and around Mare Marginis (Figure 3) constitute the western end of the swirl belt described by *El-Baz* [1972] and *Schultz and Srnka* [1980]. Goddard A, a fresh ~12 km diameter crater just north of Mare Marginis, was proposed by *Schultz and Srnka* [1980] to have been formed by the impact of the nucleus of a comet whose coma produced the swirls in this area. The Marginis swirls can be seen in Apollo 16 image AS16-121-19430 and appear on maps by *El-Baz* [1972], *Wilhelms and El-Baz* [1977], *Schultz*

and *Srnka* [1980], and *Hood and Williams* [1989]. A highland unit, “furrowed and pitted material” of Imbrian or Nectarian age, has been mapped immediately to the north and east of Mare Marginis [*Wilhelms and El-Baz*, 1977]. Furrowed and pitted terrain, which has some morphological similarities to the grooved and mounded unit near Mare Ingenii (see section 3.2 above), occurs near the antipode to the Orientale basin and the two units may share an origin in the deposition of antipodal basin ejecta [*Moore et al.*, 1974; *Wieczorek and Zuber*, 2001] or antipodal seismic modification [*Schultz and Gault*, 1975]; see also discussion of the furrowed and pitted unit by *Richmond et al.* [2005].

[16] The Clementine color-composite mosaic (Figure 3) shows the bright rays surrounding Goddard A, as well as the swirls on Mare Marginis (to the west and southwest of Goddard A). In addition, on the highlands ESE of Goddard A, well-developed sinuous, curvilinear high-reflectance swirls with dark lanes are visible. *Gillis and Spudis* [2000] conducted a geological study of the Marginis-Smythii region. They examined the Marginis swirls using Clementine parameter maps and attributed the high albedo of the swirls to the presence of unweathered material, but could not distinguish between swirl origin by magnetic shielding and scouring by comet impact.

[17] Lunar Prospector coverage of the Marginis area is relatively poor. Maps by *Richmond et al.* [2005], *Richmond and Hood* [2008a], and the Apollo subsatellite maps of *Hood and Williams* [1989] show a somewhat “lumpy” field here. The largest anomaly in this group is nearly centered on Goddard A, and has an estimated amplitude at 30 km of 6 nT.

4. Magnetic Anomalies Identified from Orbit

[18] In this section we present two magnetic anomalies and associated albedo markings that have been the subject of previous study (Descartes and Airy). We then examine five other lunar crustal magnetic anomalies in order to determine if unusual albedo features are also present. The Rima Sirsalis magnetic anomaly has been known since Apollo, while anomalies near Abel, Crozier, Hartwig, and Stöfler have only recently been revealed through processing of Lunar Prospector data [*Richmond and Hood*, 2008a].

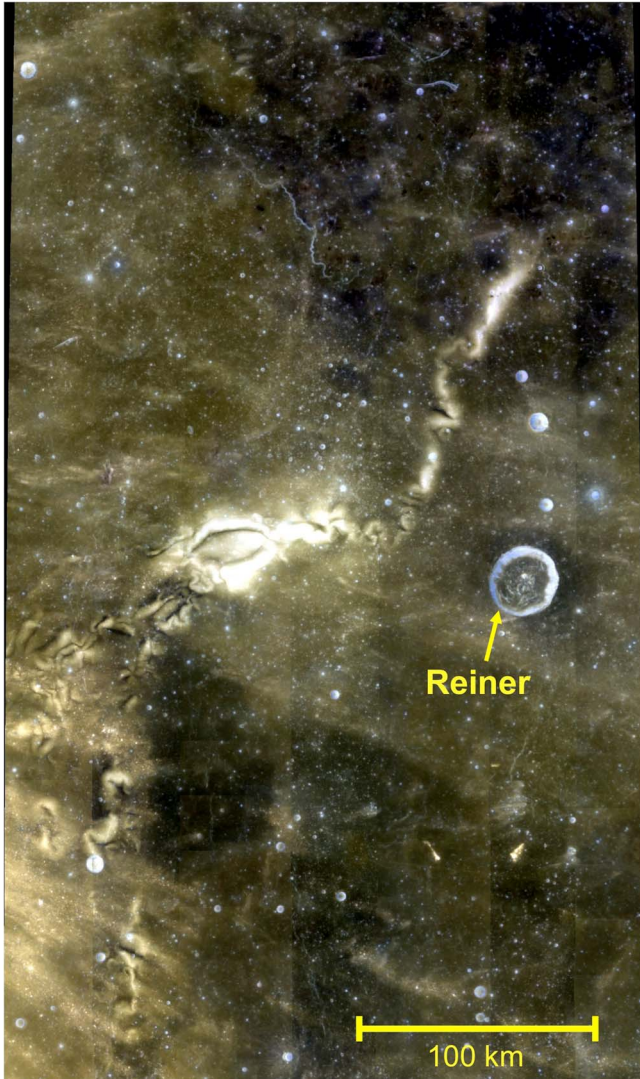


Figure 1. The Reiner Gamma Formation, the type occurrence of a lunar swirl. Clementine color composite image covers 0.125°N – 14.875°N , 298.12°E – 306.87°E in sinusoidal projection. Color assignments are red plane (R) = 950 nm filter, green (G) = 750 nm, and blue (B) = 415 nm.

4.1. Descartes

[19] A crustal magnetic anomaly in the Descartes mountains south of the Apollo 16 landing site was identified through analysis of Lunar Prospector electron reflectometer data [Halekas et al., 2001]. Mapping of the anomaly with Lunar Prospector magnetometer data was presented by Richmond et al. [2003], who noted that a diffuse area of high reflectance coincides with the magnetic anomaly. This high-albedo area (Figure 4) had previously been described and was once considered as a candidate for highland volcanism [Milton, 1968; Wilhelms and McCauley, 1971; Head and Goetz, 1972]. Richmond et al. [2003] attributed the high albedo to decreased space weathering by the solar wind deflection mechanism and suggested that the source of the magnetic anomaly is magnetized ejecta (Cayley and Descartes Formation materials) from the Nectaris or Imbrium basins. Radioisotope dating of Apollo 16 breccias suggests

that the Descartes terrain was emplaced as Imbrium basin ejecta [Norman et al., 2010].

[20] Blewett et al. [2005] discussed the case of the Descartes magnetic and albedo anomaly, and pointed out that the presence of two fresh impact craters and radar characteristics consistent with a high abundance of centimeter-to-decimeter-size surface scatterers [Zisk et al., 1972] could account for the high albedo, even without anomalous space weathering caused by magnetic shielding of the surface from solar wind sputtering and implantation. However, the coincidence of the high-reflectance spot with the magnetic anomaly is strongly suggestive that the two are related. It is attractive to consider it as an end-member swirl type that is characteristic of the highlands [Blewett et al., 2007b].

[21] The magnetic anomaly is the strongest on the lunar nearside, slightly stronger than the one at Reiner Gamma [Richmond et al., 2003; Richmond and Hood, 2008a]. Interpolating the maximum amplitudes of the Descartes anomaly in Lunar Prospector magnetometer orbit passes at 19 and 35 km altitude yields an estimated total field strength at 30 km of 24 nT.

4.2. Airy

[22] An isolated magnetic anomaly is found in the near-side highlands just west of Airy crater [Blewett et al., 2007b; Richmond and Hood, 2008a; Purucker, 2008]. The area is mapped as Imbrian-aged smooth plains and rolling terra material [Holt, 1974]. Blewett et al. [2007b] described a high-reflectance marking that coincides with the magnetic

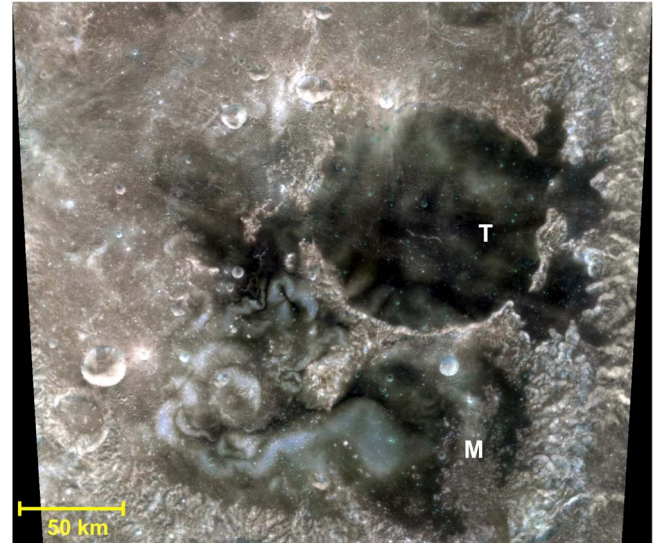


Figure 2. The Mare Ingenii swirls, in the vicinity of the Imbrium basin antipode. Image covers 29.12°S – 37.87°S , 158.12°E – 169.87°E in sinusoidal projection. Color assignments are as in Figure 1. Label T denotes the mare-flooded crater Thomson (117 km diameter); M is Thomson M, the large, partially mare-filled crater immediately south of Thomson. An area of grooved and mounded texture [Stuart-Alexander, 1978] is present along the right edge of the image. Portions of the scene missing data in one of the spectral bands have been filled in with pixels from other bands.

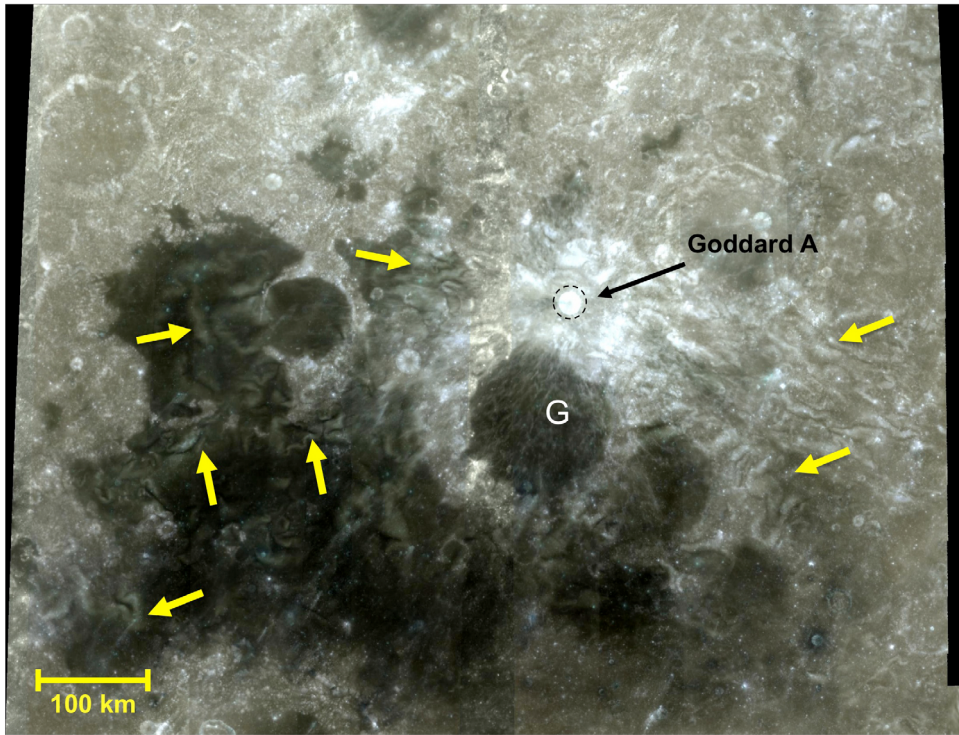


Figure 3. The Mare Marginis swirls, in the vicinity of the Orientale basin antipode. Image covers 10°N–22°N, 80°E–96°E in sinusoidal projection. RGB color assignments are R = 900 nm, G = 750 nm, and B = 415 nm. Label G denotes the mare-flooded crater Goddard (89 km diameter). Arrows point out swirls on mare and highlands. Portions of the scene missing data in one of the spectral bands have been filled in with pixels from other bands.

anomaly (Figure 5). The Airy albedo feature ($\sim 18.1^\circ\text{S}$, 3.25°E) consists of an elongated, curved bright area (originally interpreted as ray material by Holt [1974]) with a narrow, central darker portion. Analysis of Earth-based telescopic near-infrared reflectance spectra and Clementine multispectral images for the albedo markings demonstrate that the high reflectance is a result of a contrast in optical immaturity compared to the surroundings, with no indication of unusual composition [Blewett et al., 2007b]. The single loop with central dark lane structure is interpreted as an intermediate swirl form, between the simple diffuse high-albedo spot of the Descartes anomaly and the complex looping, sinuous high-albedo/dark lane patterns of swirls such as Reiner Gamma.

[23] In order to determine the magnetic anomaly strength at 30 km altitude, the individual orbit tracks used to produce the contour map shown Blewett et al. [2007b] were examined. This estimate gives an intensity of 13 nT. Airy's magnetic strength falls into our "moderate" category (Table 1).

4.3. Rima Sirsalis

[24] Rima Sirsalis (Figure 6) is a 300 km long straight rille located at $\sim 13^\circ\text{S}$, 59°W . It extends in the highlands across distal Orientale ejecta northeast toward Oceanus Procellarum [Schultz, 1976]. The Rima Sirsalis magnetic anomaly was first identified by Anderson et al. [1977] using Apollo 16 subsatellite electron reflectometer data. Srnka et al. [1979] performed modeling of the magnetic anomaly, assuming the rille was the magnetized body responsible for the anomaly. Lunar Prospector mapping provided more details of

the Rima Sirsalis anomaly [Halekas et al., 2001; Hood et al., 2001, Richmond and Hood, 2008a; Purucker, 2008]. Hood et al. [2001] found that the magnetic anomaly is not centered on the rille itself, but rather on an Imbrian aged smooth plains unit slightly to the southeast of the rille. Hood et al. [2001] suggested that the plains unit (Ip on the map of McCauley [1973]) was the source of the Rima Sirsalis anomaly, because of the association of other Imbrian-age basin ejecta units with magnetic anomalies (e.g., Cayley and Descartes materials near the Apollo 16 site, Richmond et al. [2003]). Halekas et al. [2001], who sought correlations between 77 other nearside rilles and magnetic anomalies but found none, support the conclusion of Hood et al. [2001] that the plains unit, not the rille, is the source of the magnetic anomaly. The magnetic contour map of the Sirsalis area, from Purucker [2008] (Figure 6a), is similar to that of Hood et al. [2001], with a primary anomaly centered immediately east of the rille and a secondary anomaly to the northeast near the mare-flooded crater Sirsalis E. The peak magnetic field strength in our map is just under 8 nT, in agreement with estimates made from examination of the individual orbit passes employed in production of the map.

[25] Our study of images for the region has identified one classic sinuous swirl-like marking to the north of Sirsalis at $\sim 1^\circ\text{S}$, 61°W (Figure 6b) and a loop with a dark lane northeast of Sirsalis within the secondary magnetic anomaly ($\sim 7^\circ\text{S}$, 53.5°W , Figure 6c); both of these features are on mare material in Oceanus Procellarum. Potential anomalous

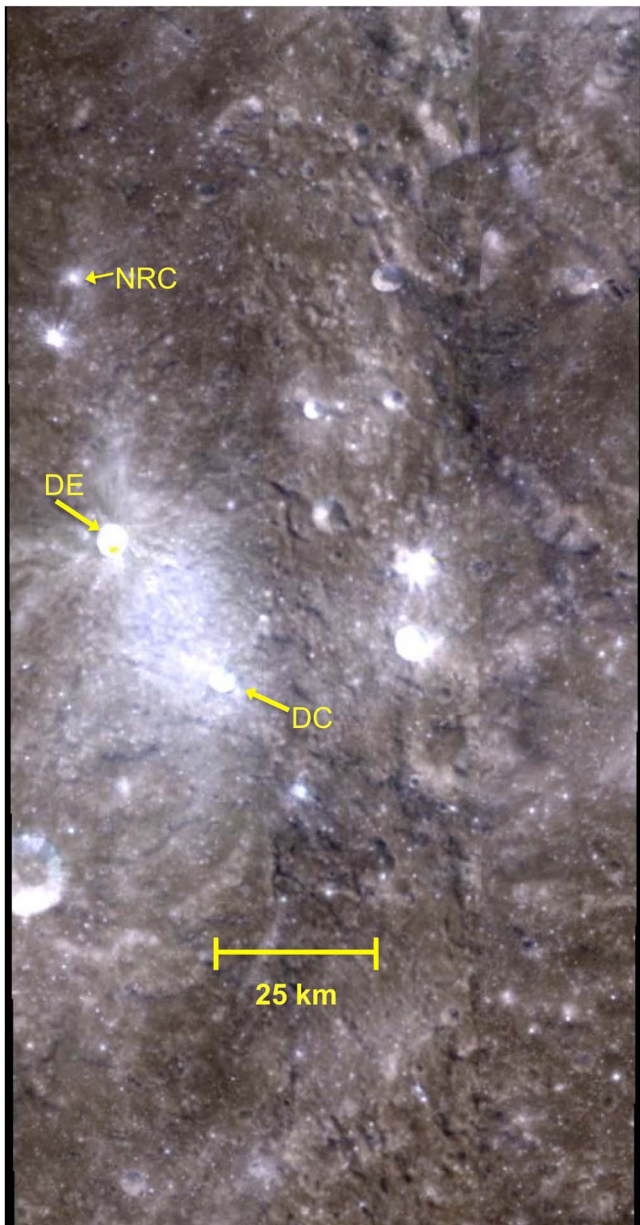


Figure 4. The Descartes albedo anomaly. Image covers 7°S – 14°S , 15.125°E – 18.625°E in sinusoidal projection. Color assignments are as in Figure 1. Label NRC = North Ray Crater (Apollo 16 site), DE = Dollond E, and DC = Descartes C. The albedo anomaly is the bright region between DE and DC.

loops and bright patches ($\sim 15^{\circ}\text{S}$, 59°W ; Figure 6d) on the highland plains unit close to the primary magnetic anomaly have also been located.

[26] The swirl at 1°S , 61°W has the shape of the Greek letter omega (Ω , Figure 6b) and is just east of crater Lohrmann A. In our map, the field strength over the omega swirl is ~ 1 nT, though at the surface the field could be stronger (see section 6). This albedo feature was mentioned in the Lunar Photo of the Day (available at www.lpod.org) for 04 April 2009, where it was described as a “swirlette” that possibly represented an extension of Reiner Gamma’s southern tail. The distance from the omega swirl to the main

Sirsalis magnetic anomaly is ~ 352 km, and its distance from the main Reiner Gamma magnetic anomaly is ~ 268 km. Hood *et al.* [2001] suggested that both the Reiner Gamma and the Sirsalis magnetic anomalies result from magnetized Imbrium ejecta, so the omega swirl could be a link between these two.

[27] The loop and dark lane at 7°S , 53.5°W have several associated wispy elongated high-reflectance patches (Figures 6a and 6c). A number of bright crater ray segments, likely from Sirsalis and Sirsalis F, cross this portion of the mare. Despite the distraction caused by these rays, the loop and dark lane structure is clear, with a morphology similar to other swirls found on the maria and to the highland high-albedo loop coincident with the Airy magnetic anomaly (section 4.2 above). The Lunar Prospector magnetic map (Figure 6a) shows the field strength at this loop, within the secondary Sirsalis anomaly, to be 3–5 nT at 30 km altitude.

[28] In the highlands, swirls typically have less albedo contrast and less-complex morphology than those on the maria. Hood [1981] remarked on possible swirl markings around Sirsalis F and J. The bright rays of the Copernican crater Sirsalis F complicate interpretation of features on the plains unit within the main Sirsalis magnetic anomaly. Several markings that have shape and color characteristics similar to albedo patterns associated with other highland magnetic anomalies are visible between Sirsalis J and Fontana C (in the peak of the primary magnetic anomaly) in the high Sun Clementine color-composite image. However, examination of Lunar Orbiter 4 frame 156-H2, which has lower Sun illumination, suggests that the high-albedo markings between these

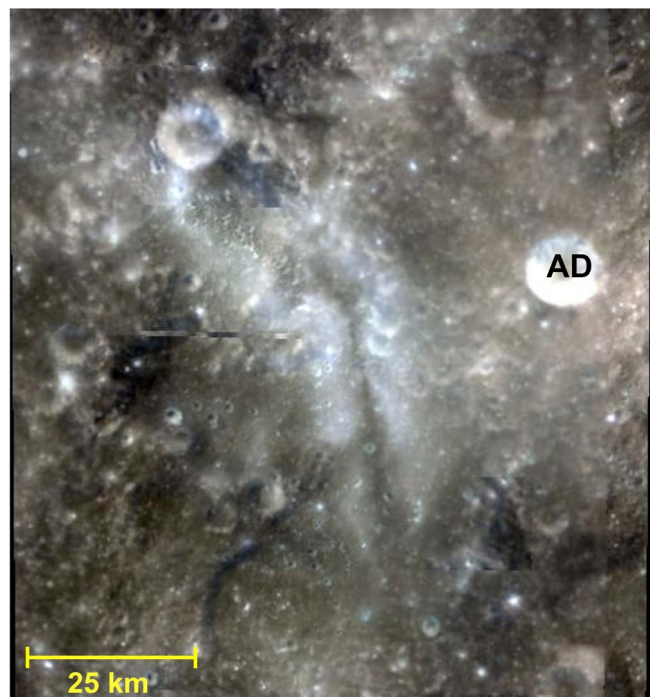


Figure 5. The albedo anomaly near Airy crater. Image covers 16.12°S – 19.87°S , 1.625°E – 4.875°E in sinusoidal projection. RGB color assignments are as in Figure 1. The loop-with-dark lane albedo feature is visible in the center of the image. Label AD is crater Argelander D. Airy crater is centered just to the east of this view.

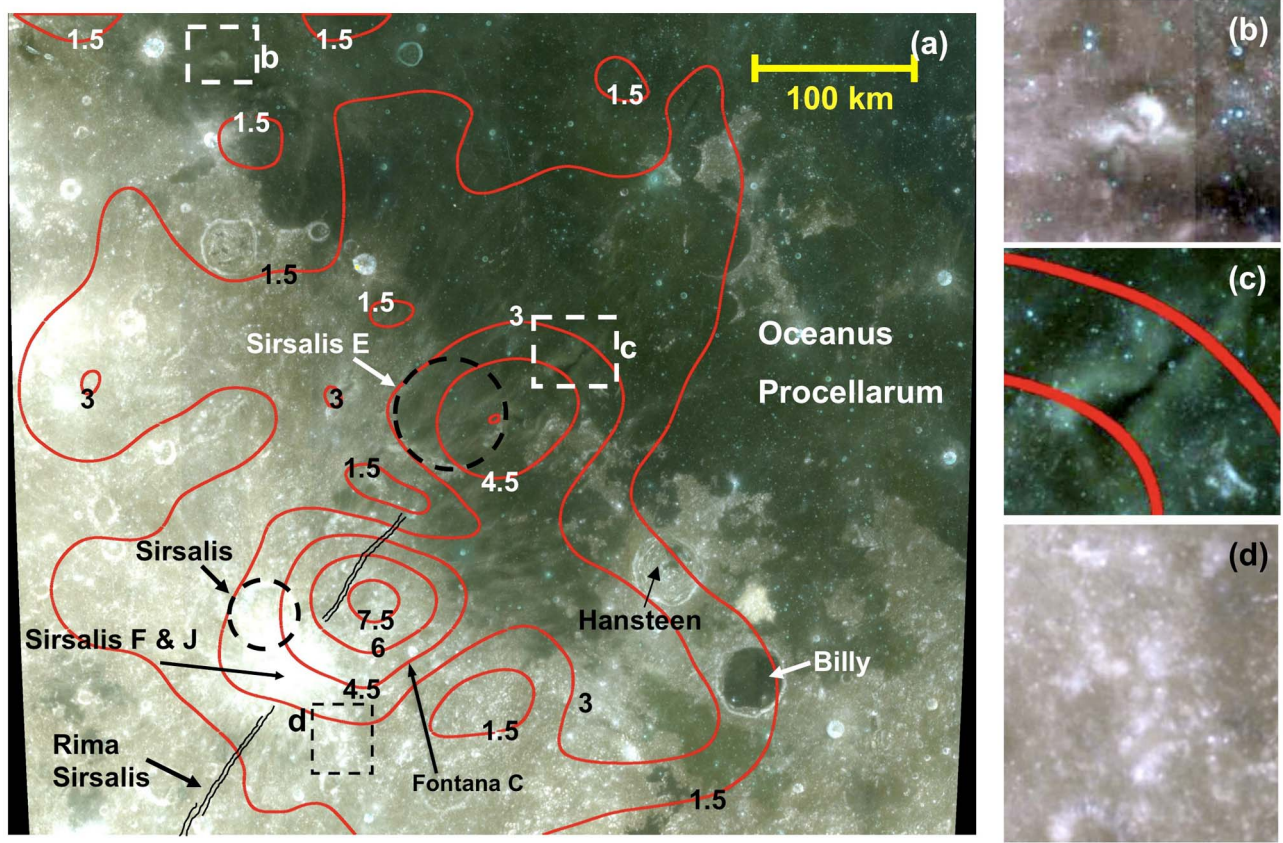


Figure 6. The Rima Sirsalis magnetic and albedo anomalies. (a) Image covers 0°S – 17°S , 294.5°E – 314.5°E in sinusoidal projection. RGB color assignments are $R = 1000\text{ nm}$, $G = 750\text{ nm}$, and $B = 415\text{ nm}$. Contours, labeled in nanoteslas, are Lunar Prospector scalar magnetic field strength continued to 30 km altitude [Purucker, 2008]. Detail of small swirls in dashed boxes b, c, and d in Figure 6a are shown in (b), (c), and (d) images, at right.

two craters could be the result of topographic variation and ballistic shadowing of ejecta from Sirsalis F. It may be that the extensive deposition of extremely fresh material during the formation of Sirsalis F rays has overwhelmed preexisting swirl-like features in this area.

4.4. Abel

[29] *Richmond and Hood* [2008a] reported a magnetic anomaly near the crater Abel. The magnetic field map [Purucker, 2008] indicates that the anomaly is centered at $\sim 32^{\circ}\text{S}$, 88°E , on a highland promontory between Abel and Barnard D, in the northern portion of Mare Australis. The maximum strength of the feature at 30 km altitude, estimated from orbital passes in July and April 1999, is 10 nT . The origin of the magnetized crustal material here is uncertain. No recognized basin is antipodal to this location. The highland units present are Nectarian mantled and cratered terra [*Wilhelms and El-Baz*, 1977].

[30] *Richmond and Hood* [2008a] noted that no swirl-like albedo markings were mapped at this location by *Wilhelms and El-Baz* [1977]. Our examination of Clementine (Figure 7) and Lunar Orbiter images (in particular Lunar Orbiter 4 image 009-H3) found no clear examples of high-albedo patches similar to those at other swirl locations. No sinuous markings are present on the various mare units in the vicinity of the

magnetic anomaly. A few bluish, high-reflectance streaks can be seen on the highlands, but they appear to be portions of long ray segments that cross the area. No Airy-type highland loop or dark lane features are present.

4.5. Crozier

[31] An isolated magnetic anomaly exists in southern Mare Fecunditatis, near the crater Crozier [*Richmond and Hood*, 2008a]. The area (Figure 8) consists of pre-Imbrian crater material and Imbrian terra [*Hodges*, 1973]. The mare basalts surrounding this patch of highlands, as well as the mare inside Crozier (22-km diameter) and within nearby craters of similar size, are of Imbrian age [*Hodges*, 1973].

[32] The peak of the magnetic anomaly is located a short distance southeast of Crozier, approximately on crater McClure D. Individual Lunar Prospector orbital passes from July 1999 allow the strength of the anomaly, continued to 30 km altitude, to be estimated as 6 nT . The area of the peak appears to be brighter than the surrounding area. However, the area beneath the magnetic peak consists of exposed highlands, and the vicinity of Crozier has been affected by crater rays from Langrenus (127 km diameter), which is centered $\sim 250\text{ km}$ to the northeast of Crozier. Rays from Petavius B to the south and other craters also cross the area. Numerous small craters (a few kilometers in diameter and

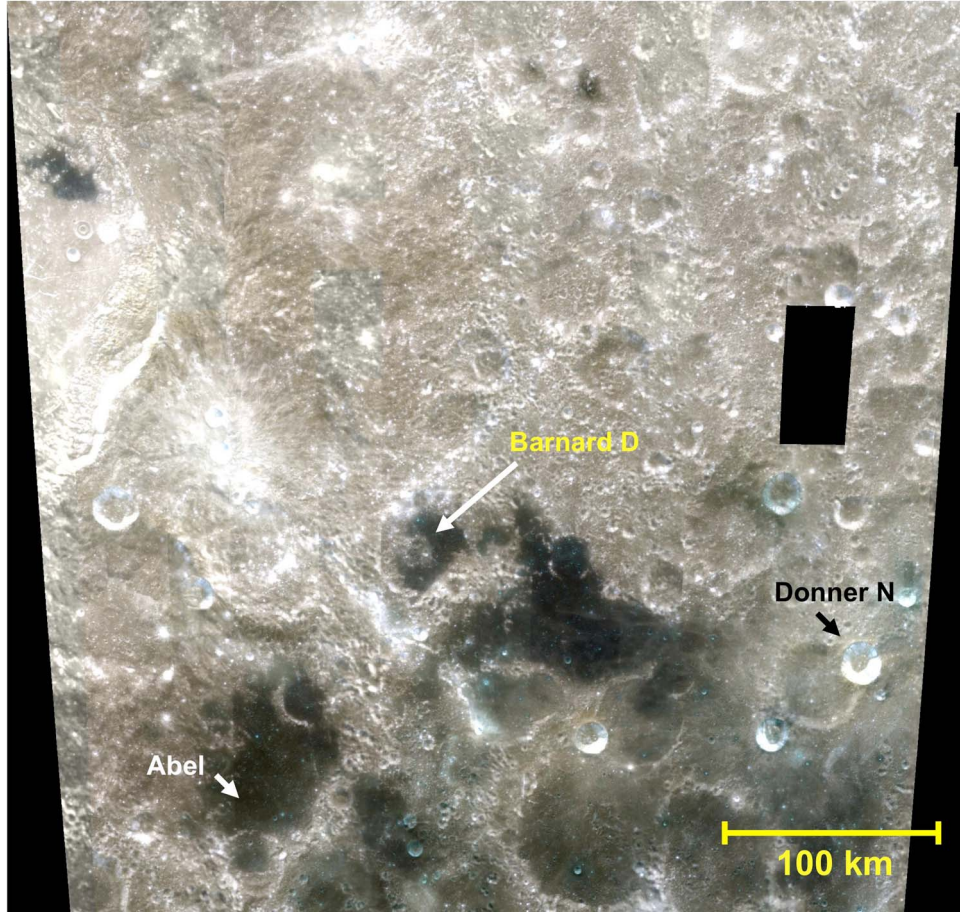


Figure 7. The area of the Abel magnetic anomaly. Image covers 23°S–37°S, 82°E–98°E in sinusoidal projection. RGB color assignments are as in Figure 1. This is an area of moderate crustal magnetism that lacks swirl-like albedo markings. Portions of the scene missing data in one of the spectral bands have been filled in with pixels from other bands.

smaller) have excavated through the highland-rich ejecta and ray materials and exposed the underlying mare basalt. These small craters are visible in the Clementine color-composite image as bluish spots with dark haloes (Figure 8). Study of the Clementine mosaic at different contrast stretches does not reveal any definitive candidate swirl-like markings in the area around Crozier. This conclusion is supported by examination of Lunar Orbiter 4 image 60-H2, which was collected at a lower Sun angle than the high-Sun Clementine view. All the high-reflectance markings can be attributed to ordinary crater rays.

4.6. Hartwig

[33] Hartwig is a degraded 79 km diameter crater just outside the Orientale basin's Cordillera mountain ring, adjacent to the crater Schluter. The isolated magnetic anomaly discovered by *Richmond and Hood* [2008a] is centered at ~8.8°S, 280.3°E in the map of *Purucker* [2008] (Figure 9a), slightly south of Hartwig and east of Schluter A. *Scott et al.* [1977] mapped the area as predominantly the inner facies of the Hevelius formation, that is, the continuous ejecta of the Orientale basin.

[34] A check of individual Lunar Prospector orbit passes from July 1999 provides an additional estimate of the maximum amplitude of the magnetic anomaly and confirms a

peak strength of ~12 nT at 30 km altitude. Despite the moderate strength of the Hartwig magnetic anomaly, swirl-like features are not readily apparent. The surface formed by Orientale ejecta at this location is strongly textured, with basin-radial ridges and troughs and ropy lobes and tongues [*Scott et al.*, 1977], as illustrated in the Lunar Orbiter view in Figure 9b. This texture combined with the presence of rays from several small, fresh craters inhibits identification of anomalous albedo patches. Portions of the area within the 10 nT contour peak of the magnetic anomaly exhibit slightly enhanced reflectance (Figure 9a) that could be related to magnetic shielding or some other special effect, but it is not possible to rule out ordinary crater rays as the cause. No unusual high-albedo markings stand out on the small mare deposits in the vicinity (Lacus Autumni and the deposit within Schluter).

4.7. Stöfler

[35] Another isolated magnetic anomaly reported by *Richmond and Hood* [2008a] is that in the southern nearside highlands near the crater Stöfler (~41.1°S, 6.0°E). The map of contoured magnetic intensity, derived from *Purucker* [2008] (Figure 10), has a broad maximum with two peaks. One peak is over Stöfler's northwest rim and the other is roughly 100 km north of Stöfler's center. An estimate made from examination of the individual orbit passes (April 1999)

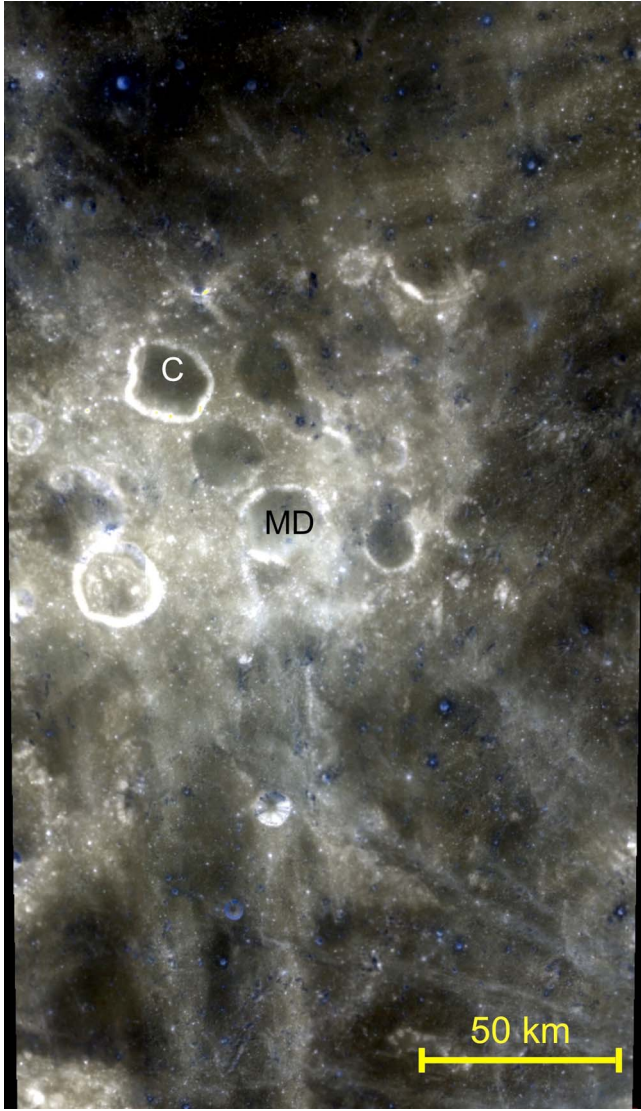


Figure 8. The area of the Crozier magnetic anomaly. Image covers 10.125°S – 19.875°S , 49.125°E – 54.875°E in sinusoidal projection. RGB color assignments are as in Figure 1. Label C is crater Crozier; MD is McClure D. No swirl-like markings have been positively identified on either the maria or highlands in the vicinity of this crustal magnetic anomaly.

confirms a maximum strength for the northern anomaly of ~ 10 nT at 30 km altitude.

[36] This portion of the nearside is dominated by pre-Imbrian crater materials, Imbrian-age craters, and Imbrian-age plains units [Pohn, 1972]. Stöfler is approximately 300 km east of the Copernican-age crater Tycho, and Tycho rays cross the area. Tycho's rays and the frame boundaries in the Clementine mosaic (Figure 10) make it more difficult to discern any swirl-like albedo patterns that could be linked to the presence of the magnetic anomaly, but no markings appear to be obviously anomalous.

5. Little-Studied Swirls

[37] In this section, we describe several previously known swirls (at the Crisium and Serenitatis antipodes, Hopmann,

Western Mare Moscovense, and Firsov) that have been the subject of only limited prior scrutiny. The existence of magnetic anomalies near the location of the Serenitatis antipode swirls was discovered using Apollo data [e.g., Lin *et al.*, 1988], but the relationship between the swirls and the magnetic anomaly has not previously been examined in detail (unlike the Orientale and Imbrium antipodes discussed above and by, for example, Lin *et al.* [1988], Hood *et al.* [2001] and Richmond *et al.* [2005]). For Hopmann, Western Mare Moscovense, and Firsov, we perform the first inquiry as to whether regions of magnetized crust are present at the locations of the anomalous high-albedo markings.

5.1. Gerasimovich

[38] Gerasimovich crater lies in the farside highlands west of the Orientale basin, just at the fringe of the Outer Hevelius Formation [Scott *et al.*, 1977]. This area was poorly covered by Lunar Orbiter and Apollo photography. Schultz and Srnka [1980], Hood [1981], and Hood and Williams [1989] mapped swirls in and around Gerasimovich with a photo returned by the Soviet Zond-8 spacecraft. The Zond image appears in Hood [1981], Hood *et al.* [2001], and Richmond *et al.* [2005]. Prior to the Clementine mosaic in Figure 11, the Zond photo was the only published image of the swirls near Gerasimovich. Hood [1981] also presented a sketch map of the swirls in the Zond photo. The swirls here consist of high-albedo patches whose morphology and color in the color-composite image differ from the crater rays originating from small, fresh craters nearby (Figure 11). The enigmatic high-albedo patches in and near Gerasimovich do not display the more-complicated sinuous shape of the highland swirls near Mare Marginis. Rather the Gerasimovich features appear as atypical high-albedo patches, with some that are of the simple loop-with-dark lane style similar to the example near Airy crater (section 4.2 above) and some of the markings near Firsov (section 5.5, below).

[39] The magnetic anomaly near Gerasimovich is the strongest yet identified on the Moon [Hood *et al.*, 2001; Richmond *et al.*, 2005; Richmond and Hood, 2008a]. The structure has two strong peaks, as seen in the maps by Hood *et al.* [2001], Richmond and Hood [2008a], and Purucker [2008]. The northern peak is located at $\sim 20.5^{\circ}\text{S}$, 237°E , about 100 km NNW of Gerasimovich D. The peak to the southeast is at $\sim 23^{\circ}\text{S}$, 239°E , just southeast of the rim of Gerasimovich D. The strengths of these peaks at 30 km altitude, determined from Lunar Prospector orbital passes in April and May 1999, are estimated to be 28 nT (northern) and 23 nT (southeastern). The swirl-like markings (Figure 11) are found within the areas of peak field strength. Observations of magnetic fields by the Lunar Prospector electron reflectometer [Halekas *et al.*, 2008] and of backscattered neutral hydrogen by the Chandrayaan-1 spacecraft [Wieser *et al.*, 2010] demonstrate that a minimagnetosphere exists over the Gerasimovich magnetic anomaly.

5.2. Northwest of Apollo Basin

[40] Farside swirls northwest of the Apollo basin were mapped by Schultz and Srnka [1980] and Hood and Williams [1989]. Hood and Williams [1989] showed Lunar Orbiter 1 frame 38-M and pointed out “relatively indistinct” swirl-like markings, noting that the illumination conditions were poor. The highland units here consist of Nectarian and

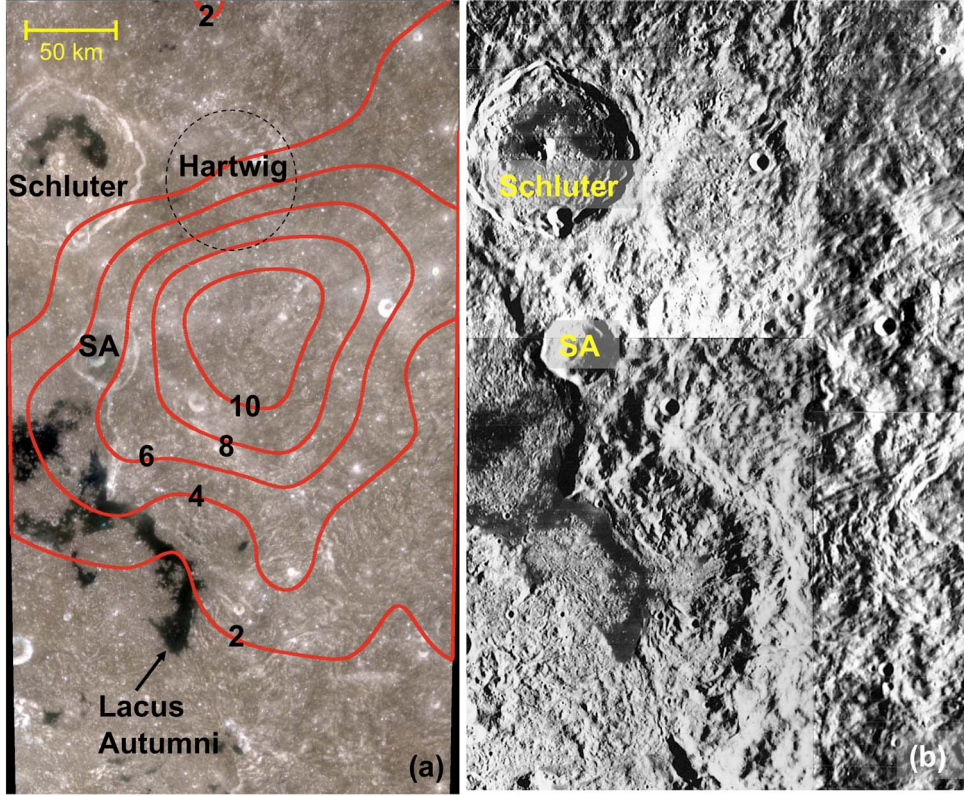


Figure 9. The Hartwig magnetic anomaly. Image covers 3°S–17°S, 276°E–284°E in sinusoidal projection. (a) Clementine color composite with RGB color assignments as in Figure 1. Contours are as described in Figure 6 caption. Crater Schluter A is labeled SA. (b) Lunar Orbiter 4 mosaic covering the same area as the Clementine image in Figure 9a, illustrating the texture of Orientale basin ejecta at this location. No swirl-like markings have been definitively identified on either the maria or highlands in the vicinity of this crustal magnetic anomaly.

pre-Nectarian terrae, with small ponds of Imbrian light plains [Stuart-Alexander, 1978]. This area is antipodal to the Serenitatis basin (geometrical antipode at 26°S, 198°E, assuming the basin center given by Spudis [1993]). Grooved massifs visible in Lunar Orbiter frames are similar to terrain at the Imbrium and Orientale antipodes [Wilhelms, 1987, Figure 9.21A], though he notes that the grooves could have been formed by secondary impacts from nearby basins. The location of these grooves is indicated in the Clementine mosaic of Figure 12. The potential swirls noted by previous workers (arrows, Figure 12) are found in the area roughly bounded by Lacus Oblivionis and craters Walker and Rumford. These high-albedo markings are of moderate sinuosity, with the presence of some dark lanes.

[41] A series of crustal magnetic anomalies roughly at the Serenitatis antipode appear on maps presented by Lin *et al.* [1988], Hood and Williams [1989], Richmond and Hood [2008a], and Purucker [2008]. The swirls coincide with the area of the peak magnetic strength, which at 30 km altitude is estimated using individual orbital passes to be ~12 nT. The Serenitatis antipode is somewhat similar to that of the Crisium basin (Gerasimovich area): a highland region with a moderate or strong crustal magnetic anomaly and anomalous high-reflectance markings that do not display the prominence or fully-developed complex geometry of the Reiner Gamma or Ingenii swirls.

5.3. Hopmann

[42] Hopmann crater (88 km diameter, 50.8°S, 160.3°E), is located in the farside highlands in an area of poor coverage by Lunar Orbiter photographs. Of Nectarian age [Wilhelms *et al.*, 1979], Hopmann has a flat, mare-flooded floor, a small central peak remnant, and terraced walls (Figure 13). The Lunar Photo of the Day for 23 July 2007 drew attention to a small swirl on the southeastern floor in the form of a narrow, tightly sinuous, high-albedo ribbon visible in the Clementine images (Figures 13a and 13c). In addition, we point out an Airy-type elongated loop with a dark lane found on the highlands just outside the crater's northeastern rim (Figure 13b), and potentially anomalous high-reflectance markings to the north, west, and east of Hopmann (yellow arrows, Figure 13a). Other nearby high-albedo patches are found on the floor of Garavito Y, and crossing Chretien S and W. The Hopmann swirls, as well as these additional markings, could be related to the major Mare Ingenii (Imbrium basin antipode) swirls that lie ~450 km to the north.

[43] A crustal anomaly at the location of Hopmann appears in the global lunar magnetic maps of Richmond and Hood [2008a] and Purucker [2008]. The peak of the magnetic anomaly is centered approximately on the bright loop in Figure 13b. Data from Lunar Prospector orbits in April and May, 1999, permit the anomaly strength at 30 km altitude to be estimated as 5 nT.

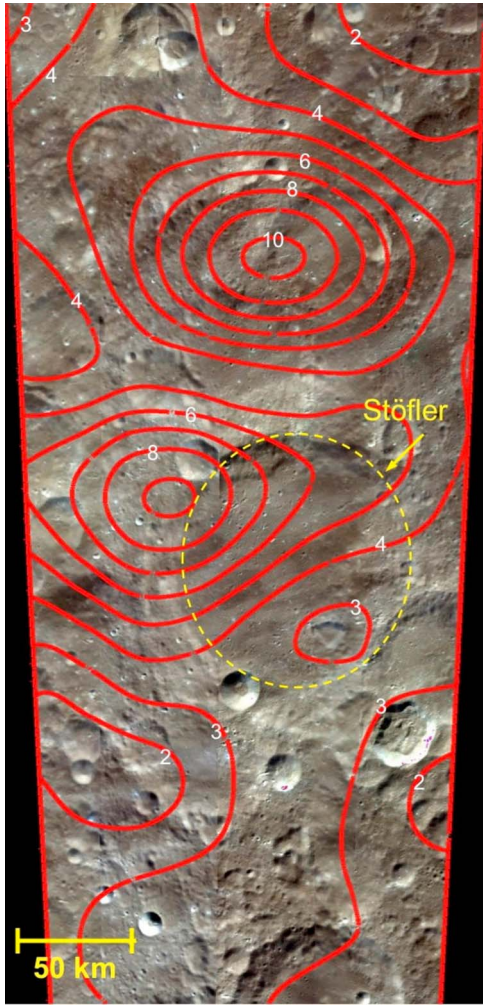


Figure 10. The Stöfler magnetic anomaly. Image covers 33°S – 47°S , 1°E – 9°E in sinusoidal projection. RGB color assignments are as in Figure 1. Contours are as described in caption to Figure 6. No swirl-like markings have been identified in association with this crustal magnetic anomaly.

5.4. Mare Moscovense

[44] The Moscovense basin is centered at 26°N , 148°E [Spudis, 1993]. Lunar swirls are located on the western portion of Mare Moscovense (Figure 14) and were previously mapped by Gillis and Spudis [1996] and Craddock *et al.* [1997]. The swirls are marginally visible in an Apollo 13 color Hasselblad frame (AS13-60-8648). The swirls exhibit a complex, sinuous morphology, though their albedo contrast against the mare background is not nearly as great as that of the mare swirls at Reiner Gamma and Mare Ingenii. The Moscovense swirls appear to be mostly confined to the mare surface. However, the contact between the mare basalts and the highland units in western Moscovense is not sharp. The swirls may extend onto units mapped as Imbrian-age plains by Stuart-Alexander [1978] or as possible pyroclastics by Craddock *et al.* [1997].

[45] Weak magnetization at Moscovense was reported by Halekas *et al.* [2003] and Richmond and Hood [2008a]. Richmond and Hood [2008a] discussed possibilities for the

origin of the weak fields found at basins such as Crisium and Moscovense. The magnetic anomalies could result from magnetization of the basins in the presence of an ancient core dynamo field. Recent work suggests thermoremanent magnetization of impact melt is responsible for the magnetic character of these basins [Wieczorek and Weiss, 2010; Hood, 2010]. Alternately, as noted by Hughes *et al.* [2006], the Moscovense swirls are located roughly at the antipode of the Humorum basin. Based on the Humorum basin center given by Spudis [1993], the Humorum antipode is located at 24°N , 141°E , or roughly 120 km southwest of the swirls. Thus, the Moscovense (Humorum antipode) magnetic anomaly may have originated by the same type of process that produced the stronger crustal fields antipodal to younger basins such as Imbrium, Orientale, Serenitatis, and Crisium. Hood's [2010] study of magnetism at Moscovense indicates that one anomaly is located near the center of the basin, and a second is found at the western edge of the mare in the vicinity of the swirl concentration. The western anomaly's strength is ~ 4 nT at 30 km altitude, estimated from Lunar Prospector orbital passes in June 1999. The central anomaly is broader, with approximately the same peak strength.

5.5. Firsov

[46] A group of farside swirls east of the crater Firsov (centered at 4.5°N , 112.2°E) form the eastern end of a belt of swirls described by El-Baz [1972] and Schultz and Srnka [1980]. The belt extends west to the vicinity of Mare Marginis and the crater Goddard A (see section 3.3 above). Schultz and Srnka [1980] suggested the swirls were produced by the interaction of gas and dust from the coma with the regolith during a cometary collision. An Apollo 10 Hasselblad image (AS10-30-4365, Figure 15) dramatically shows the swirls on the highlands.

[47] Firsov is a pre-Nectarian crater surrounded by pre-Nectarian and Nectarian terra and plains units [Wilhelms and El-Baz, 1977]. “Bright sinuous markings” have been mapped at Firsov and extending west to Mare Marginis [Wilhelms and El-Baz, 1977]. Swirls and related markings are certainly present (Figures 15 and 16), although many of the high-reflectance features in the Clementine image can be attributed to the extensive, extremely bright rays of Necho and King craters (to the south and east, respectively). The swirls visible in the Apollo 10 image, as well as nearby swirl-like patches, have a distinctive bluish appearance in the Clementine three-band color composite image (Figure 16), which distinguishes them from the Necho and King rays in this area.

[48] Magnetic field strength maps by Richmond and Hood [2008a] and Purucker [2008] show a crustal anomaly near Firsov. Lunar Prospector magnetometer data from orbital passes in April 1999 indicate the anomaly is located at $\sim 4.7^{\circ}\text{N}$, 115°E , coinciding with the swirl group east of Firsov shown in Figure 16b. The estimated peak anomaly strength at 30 km altitude is 11 nT. The comet impact hypothesis of Schultz and Srnka [1980] holds that magnetized crust was produced by amplification of the cometary field during the impact event that produced the swirls here and at Goddard A (near Mare Marginis, see section 3.3). Hood and coworkers [e.g., Hood *et al.*, 2001; Richmond *et al.*, 2005] propose that magnetized basin ejecta is responsible

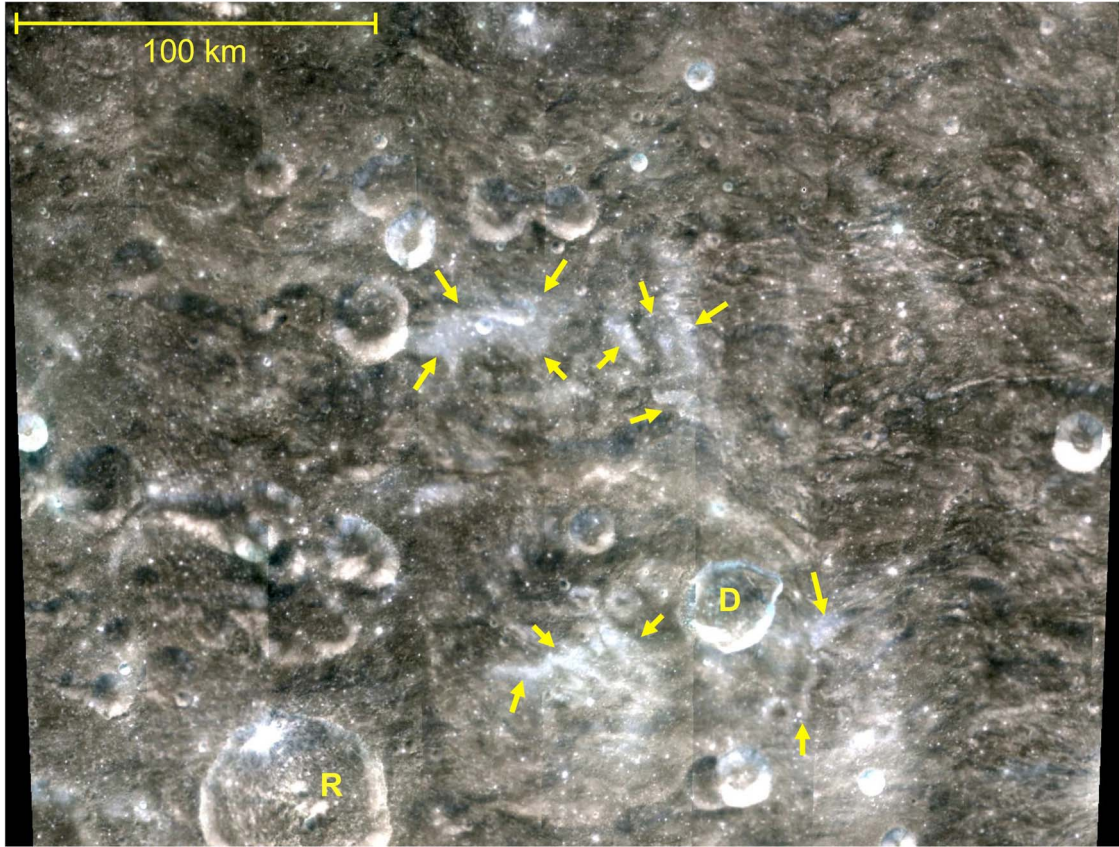


Figure 11. The Gerasimovich albedo anomaly in the vicinity of the Crisium basin antipode. Image covers 17.12°S–24.87°S, 231.12°E–241.87°E in sinusoidal projection. RGB color assignments are as in Figure 1. Label R denotes the crater Gerasimovich R (55 km diameter); D is crater Gerasimovich D. Arrows indicate swirl-like high-reflectance markings.

for the magnetic anomalies antipodal to younger basins like Orientale, Imbrium, and Crisium. The antipode of the Firsov magnetic anomaly is 5°S, 66°W, which is near the center of the Grimaldi basin listed by Spudis [1993] (6°S, 68°W). Grimaldi is small and old (pre-Nectarian), two factors that may make it less likely that Grimaldi ejecta or seismic waves contributed to magnetic effects observed at the antipode today. Instead, the Firsov magnetic anomaly could be an extension of the Orientale antipode (Mare Marginis) group. Alternately, as discussed by Richmond *et al.* [2005] and Halekas *et al.* [2002], there is some evidence that pre-Nectarian terranes are magnetic, possibly having acquired their magnetism from a core dynamo active at the time. If correct, then the magnetism in the pre-Nectarian highland units at Firsov could have originated in that way.

6. Summary of Findings for Magnetic and Albedo Anomalies

[49] The preceding sections present a comprehensive survey of lunar magnetic and albedo anomalies. Table 1 lists the locations studied, categorizes each magnetic anomaly as weak, moderate, or strong, and gives a brief description of the character of any swirl-like markings. Our findings support the conclusion of Blewett *et al.* [2007b] that crustal magnetic anomalies in the maria are correlated with albedo features that possess the complex, sinuous structure of the

Reiner Gamma Formation. Magnetic anomalies in the highlands are likely to harbor simpler high-albedo surface markings. Some areas of mixed mare/highland terrain exhibit complex swirls, and Firsov is an example of complex swirls in a pure highland setting. However, not all surfaces within weak-to-moderate magnetic anomalies have swirl-like markings. Abel, Crozier, Hartwig, and Stöfler fall into this category.

[50] The magnetic anomaly strengths presented here (maps in Figures 6, 9, and 10 and estimates listed in Table 1) are based on data obtained from orbit, and are continued to a common altitude of 30 km. Magnetic measurements made on the surface would yield greater field strengths and would likely exhibit much more complex spatial structure than is apparent from the Lunar Prospector data [e.g., Halekas *et al.*, 2010]. The presence of strong localized surface fields measured with relatively low resolution from orbit could explain the occurrence of swirl markings at locations with apparent low field strength (e.g., Moscovиense and the small swirls in Figures 6b and 13c).

7. Spectral Trends: Space Weathering and Composition

[51] In this section, we use Clementine UV-Vis multispectral image products to examine spectral relationships among selected swirls and the surrounding terrain. The goal is to provide information on composition and optical

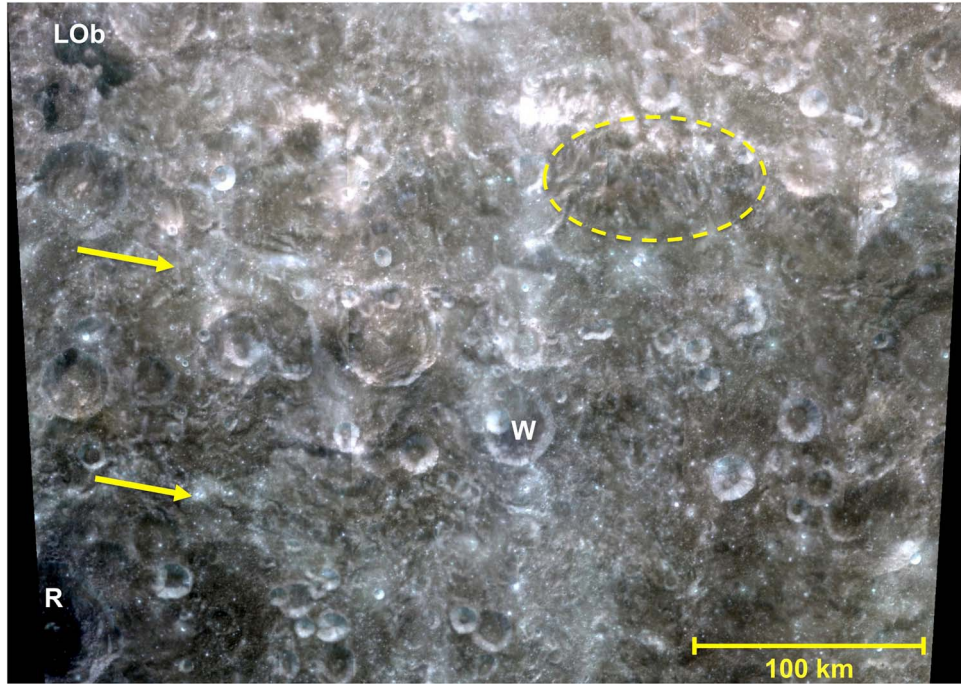


Figure 12. Swirl-like albedo anomalies northwest of the Apollo basin, in the vicinity of the Serenitatis basin antipode. Image covers 20°S–30°S, 190°E–205°E in sinusoidal projection. RGB color assignments are as in Figure 1. Lacus Oblivionis is labeled LOb, R denotes crater Rumford, and W is crater Walker (32 km diameter). Arrows indicate swirl-like high-reflectance markings. The dashed oval encloses the area of grooves discussed by Wilhelms [1987] as potentially related to the Serenitatis impact.

maturity that can be used to constrain the nature and origin of the swirls.

7.1. Background on Spectral Analysis Methods and Derived Data Products

[52] We construct maps of the ferrous iron abundance (FeO) and optical maturity parameter (OMAT) using Clementine images and the algorithms of Lucey *et al.* [2000a, 2000b]. These algorithms represent a quantification of the Hapke model for understanding the reflectance of a silicate regolith [Hapke *et al.*, 1975; Rava and Hapke, 1987]. According to this model, the reflectance properties in the near-ultraviolet to near-infrared portion of the spectrum are controlled chiefly by three components: (1) opaque phases such as ilmenite (FeTiO_3) or coarse-grained iron metal; (2) ferrous iron in transparent minerals and glasses, and (3) nanometer-to-micrometer-sized particles of metallic iron.

[53] Opaque phases that are large compared with the wavelength of light generally have low reflectance and flat spectra lacking strong absorption features. Therefore, increasing the abundance of an opaque in a soil will tend to lower the albedo across the spectrum and simultaneously cause the spectrum to become less red (“bluer”). The visible spectral slope is often measured via the ratio of reflectance in the ultraviolet or blue to the reflectance in the red or infrared. This ratio has been used for mapping titanium content via the spectral effects of ilmenite [e.g., Lucey *et al.*, 1998, 2000a].

[54] Ferrous iron (Fe^{2+}) in silicates is responsible for an electronic absorption band centered near a wavelength of 1000 nm (1 μm). The 950 nm/750 nm reflectance ratio is a measure of reflectance near the center (950 nm) of the Fe^{2+}

absorption relative to the reflectance in the continuum (750 nm). Thus, this near-infrared (NIR) color-ratio value is related to the strength of the absorption band and hence to the abundance of Fe^{2+} in the silicate material. Greater Fe^{2+} abundance (deeper band) will decrease the 950 nm/750 nm ratio. An increase in the Fe^{2+} content of a silicate mineral or glass will also cause decreased overall reflectance, as the “1 μm ” band deepens, broadens, and begins to overlap with strong charge transfer absorptions in the ultraviolet. Similarly, a decrease in 1 μm band strength related to lower Fe^{2+} abundance or caused by space weathering will increase the 950 nm/750 nm ratio. The continuum slope in the NIR also influences the 950 nm/750 nm ratio. A steeper (“redder”) slope corresponds to a higher ratio value.

[55] Submicrometer-size metallic iron particles (also called nanophase iron, npFe^0) are produced by two processes related to space weathering, the exposure of material on the surface of an airless body [e.g., Hapke, 2001; Noble and Pieters, 2003]. Micrometeoroid impacts on and solar wind sputtering of FeO-bearing material produce vapor phase deposits of small (less than ~10 nm) iron particles on the surfaces of soil grains [Keller and McKay, 1993; Pieters *et al.*, 1993]. During micrometeoroid impact melting of soil, FeO can be reduced, perhaps with the aid of implanted solar wind hydrogen, to create larger metallic iron blebs that are up to several hundred nanometers in size. The iron blebs produced during melting are found within glassy agglutinate particles. Experimental work has determined that the spectral effects of iron particles have an important dependence on size [Noble *et al.*, 2007; Lucey and Noble, 2008; and references therein]. Smaller npFe^0 (less than ~10 nm)

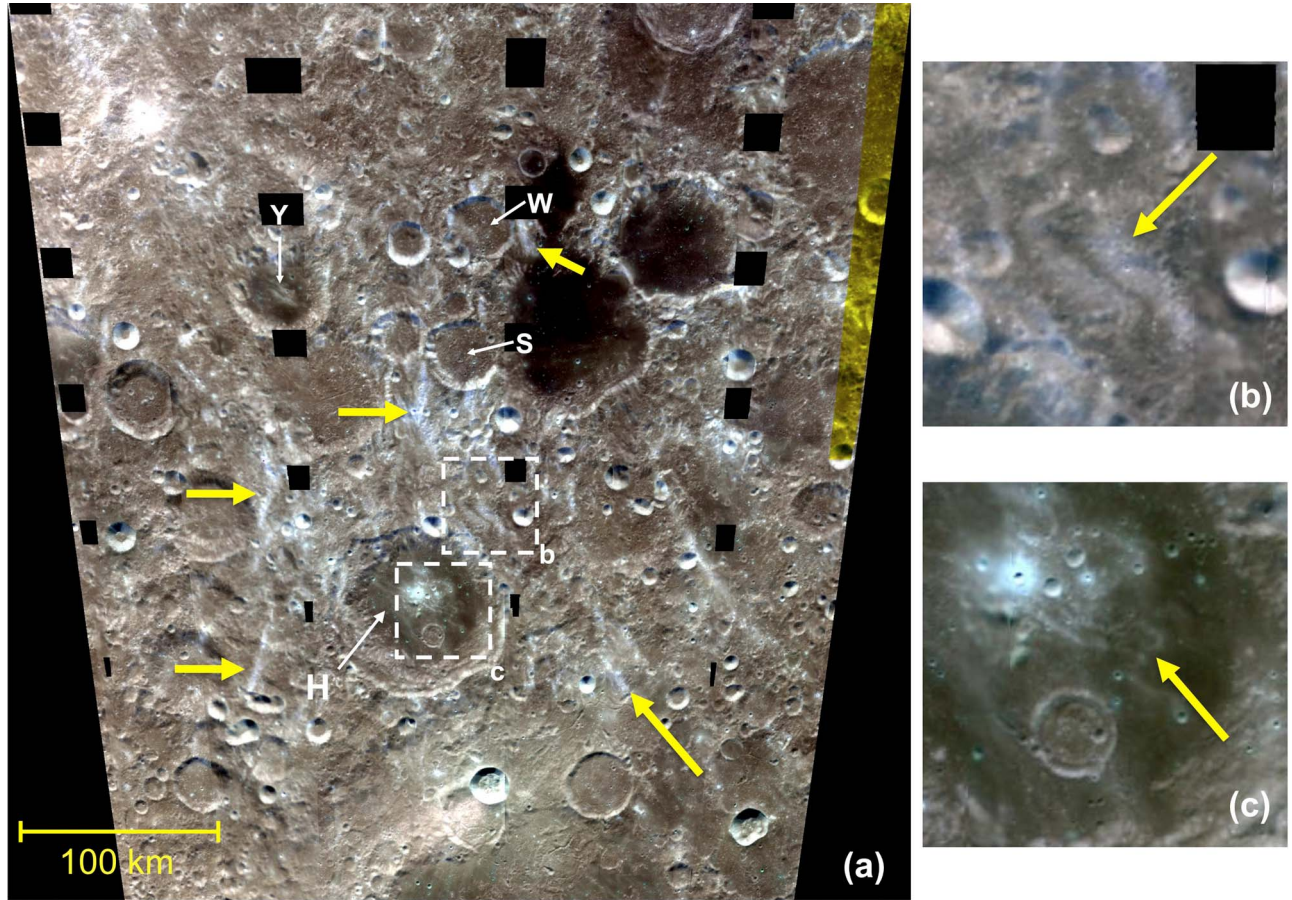


Figure 13. Swirls in and near crater Hopmann (88 km diameter; arrow at label H points to floor of Hopmann). (a) Image covers 41°S–56°S, 150°E–170°E in sinusoidal projection. RGB color assignments are as in Figure 1. Label S is crater Chretien S, W is Chretien W, and Y is Garavito Y. Thick yellow arrows point to swirls and other unusual high-reflectance markings. Dashed boxes labeled b and c in Figure 13a indicate areas included in Figures 13b and 13c, respectively. (b) Loop-with-dark lane (arrow) and other high-albedo streaks. (c) Tightly sinuous swirl (arrow) on the mare-filled southeast floor of Hopmann.

causes some darkening and also greatly affects the visible continuum, producing a strong red spectral slope. Larger (greater than ~ 50 nm) npFe⁰ tends to cause an overall reduction in reflectance, with little effect on the continuum shape. For intermediate sizes, the spectral effects depend on the concentration of npFe⁰ particles: low abundances cause a curved spectrum in the visible, and as the concentration of npFe⁰ increases, the reflectance decreases while the continuum becomes more linear and strongly sloped from visible to near-infrared. As a planetary regolith is exposed to space, it accumulates more of these weathering products and thus “matures” as a function of time. A greater abundance of small npFe⁰ will lead to a stronger red spectral slope and weaker 1 μm band, which is manifest as an increase in the 950 nm/750 nm ratio.

[56] The spectral effects of ferrous iron in silicates and the spectral effects of nanophase iron are roughly orthogonal, as illustrated in Figure 17. Increased Fe²⁺ leads to lower reflectance and lower 950 nm/750 nm ratio, whereas increased npFe⁰ (greater maturity) causes lower reflectance but higher 950 nm/750 nm ratio. The Lucey et al. [2000a, 2000b] mapping method exploits the orthogonal spectral effects of composition and maturity in order to produce parameters sensitive

to these characteristics that are decoupled from each other [see also Lucey et al., 1995, 1998; Blewett et al. 1997].

[57] We use Clementine-based maps of the OMAT and FeO parameters in the analysis below. In addition to the spectral parameter maps, we construct plots of the 950 nm/750 nm reflectance ratio versus 750 nm reflectance for image pixels within defined regions-of-interest (ROIs). Ratio-reflectance diagrams have proven to be very useful in understanding the relationships between color, composition, and space weathering on the Moon [e.g., Lucey et al., 1995, 1998; Blewett et al., 1997, Shkuratov et al., 1999; Staid and Pieters, 2000], Mercury [Robinson and Lucey, 1997; Blewett et al., 2007a, 2009; Warell and Valegård, 2006], and asteroids [Murchie et al., 2002]. Srivastava [2009] has presented a 950 nm/750 nm versus 750 nm plot for portions of the Airy and Reiner Gamma swirls as part of a study of optical maturity.

7.2. Optical Maturity and FeO Maps: General Observations

[58] The OMAT parameter is a measure of the darkening, reddening, and band depth reduction effects of the nanophase iron produced by space weathering [Lucey et al.

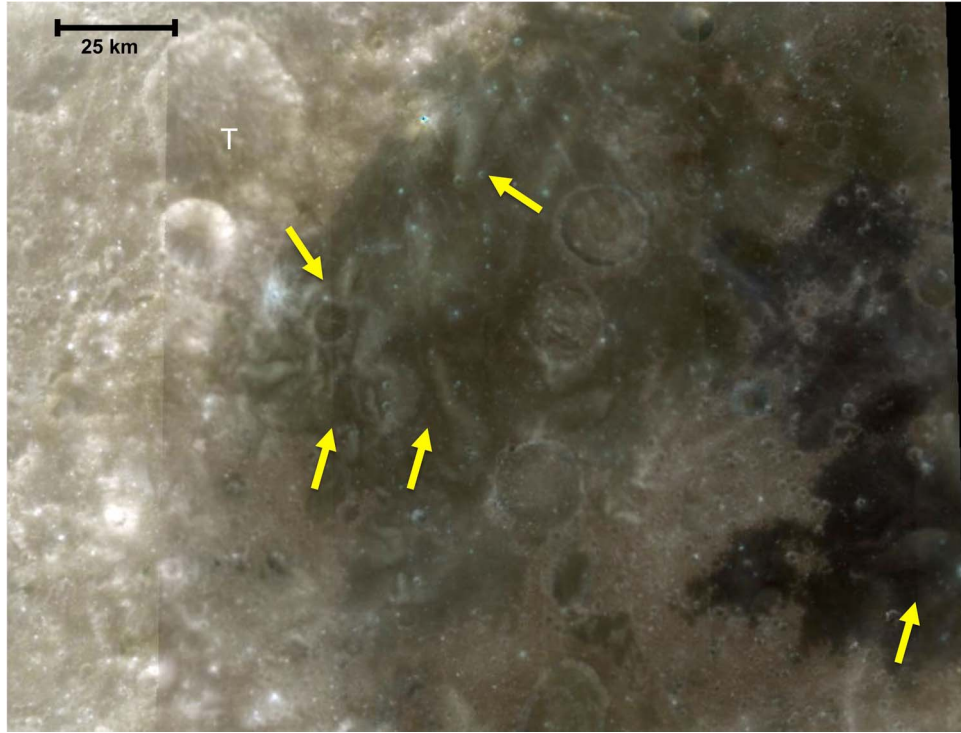


Figure 14. Swirls on western Mare Mosoviense. Image covers $\sim 24.2^{\circ}\text{N}$ – 29°N , 142°E – 149°E in sinusoidal projection. RGB color assignments are as in Figure 1. Label T is crater Tereshkova (31 km diameter). Arrows indicate high-reflectance swirls.

2000b]. The parameter is defined in such a way (Figure 17) that larger values of OMAT correspond to a lesser degree of maturity; that is, higher OMAT = immature (fresher), lower OMAT = more mature. Hence, in images of the OMAT parameter, fresh craters appear bright against a darker background of more mature material. Prior work [Hughes et al., 2006; Blewett et al. 2005, 2007b, 2007c] reported that for the locations examined, the bright portions of the swirls correspond to high OMAT values compared with the surroundings. Here we confirm that observation and find that this is the case for all swirls studied in this paper: Airy, Descartes, Firsov, Gerasimovich, Hopmann, Mare Ingenii, Mare Marginis, Mare Mosoviense, north of Rima Sirsalis, northwest of Apollo basin, and Reiner Gamma. Representative Clementine OMAT images are presented in Figures 18 to 21, where we have selected two mare swirls and two highland swirls as examples.

[59] Clementine FeO maps were constructed for all the swirls listed in the paragraph above using the algorithm of Lucey et al. [2000a]. Example images are presented in Figures 18 to 21. As a check, we also made FeO and OMAT images for Reiner Gamma using the algorithms of Wilcox et al. [2005]. This method is specifically tuned for the maria in order to provide improved suppression of maturity effects in the FeO maps. In and around the swirls, the standard and mare versions of the FeO and OMAT images are very similar, and none of our conclusions would change by employing image products generated with the Wilcox et al. [2005] algorithms.

[60] We find that at highland sites, the high-reflectance parts of a swirl are typically ~ 0 to 2 wt.% lower in FeO than

the surroundings. At mare locations the difference is slightly more pronounced, with the bright portions of a swirl ~ 1 to 4 wt.% lower in FeO than the mare background. These relatively small FeO abundance differences between swirl and background may only be marginally significant in terms of the absolute accuracy of the Lucey et al. [2000a] compositional mapping algorithm, which is on the order of ± 1 – 2 wt.% FeO. However, the fact that these contrasts are visible in the FeO images does demonstrate the presence of measurable spectral differences as quantified by ratio-reflectance values and the Lucey et al. [2000a] spectral Fe²⁺ parameter “ θ ”.

[61] In agreement with our findings, other studies have also concluded that the high albedo of the swirls is caused largely by immaturity, with a smaller contribution from compositional differences; Bell and Hawke [1981, 1987] and Pinet et al. [2000] for the Reiner Gamma Formation and Blewett et al. [2007b] for the Airy swirl. These workers used spectral evidence independent of the Lucey et al. [2000a, 2000b] mapping methods, including high-spectral resolution Earth-based telescopic data. There is no evidence that the bright swirls are composed of exotic materials or that mare swirls contain a major highland component.

[62] We have selected two mare swirls and two highland swirls to illustrate the spectral and compositional trends. The next sections examine these cases in more detail.

7.3. Reiner Gamma Formation

[63] The Reiner Gamma swirl is clearly visible in both the FeO and OMAT parameter images (Figure 18). Although not shown in the close-up view of Figure 18, the southwest



Figure 15. Lunar swirls near the crater Firsov. Apollo 10 Hasselblad image AS10-30-4365, an oblique view looking approximately north. The swirls appear to drape the topography. The crater at the top left is ~7 km in diameter. Compare with Figure 16b.

and north swirl tails have less contrast with the background and a more diffuse character in the OMAT parameter image compared with their appearance in the albedo and FeO parameter images. This could indicate that at these tail locations the visibility of the swirls is caused more by small compositional differences than by maturity contrast with the background surface.

[64] Several image ROIs for Reiner Gamma are defined in Figure 18d. The average FeO and OMAT values for each ROI are listed in Table 2. The bright portion of the central swirl has an average FeO value of ~16 wt.%, lower than those of the north and south mare background regions, which each average ~19 wt.%. The average OMAT for the bright swirl differs strongly from the averages for the two background regions, indicative of the optical immaturity of the swirl material. These compositional and maturity relations can be seen in the NIR ratio-reflectance diagram (Figure 19). The points for the main swirl lie to the upper right of the trend defined by two mare background regions. This is consistent with a slightly higher FeO abundance in the background mare, as shown by the FeO image in Figure 18c and the averages reported in Table 2. The magenta points in Figure 19, representing a transect that passes from a bright area near the center of the main swirl

southward onto the mare surface (Figure 18d), span the spectral space from the main swirl to the background mare.

7.4. Mare Ingenii

[65] The Mare Ingenii swirls are an example exhibiting complex swirl morphology. The swirls stand out easily from the surroundings in both the OMAT and FeO images (Figure 20). Two regions of interest are defined in Figure 20a. The central part of the Thomson M swirl (black outline in Figure 20a) has an average FeO value of 14 wt.% (Table 2). In the nearby Thomson M mare background (yellow outline), the average FeO is 16 wt.%. The Thomson M swirl's immaturity is evident in its average OMAT value of 0.24, much higher than that of the background mare surface, 0.16 (Table 2). These FeO and OMAT values are as expected from the locations of these regions in the NIR ratio-reflectance plot shown in Figure 21.

7.5. Descartes

[66] At Descartes (Figure 22), the high-reflectance albedo anomaly is prominent in the OMAT image and has a small difference from the nearby surface in the FeO image. The central part of the albedo anomaly (Figure 22a) has an average FeO value of 4.5 wt.% (Table 2). The area of the

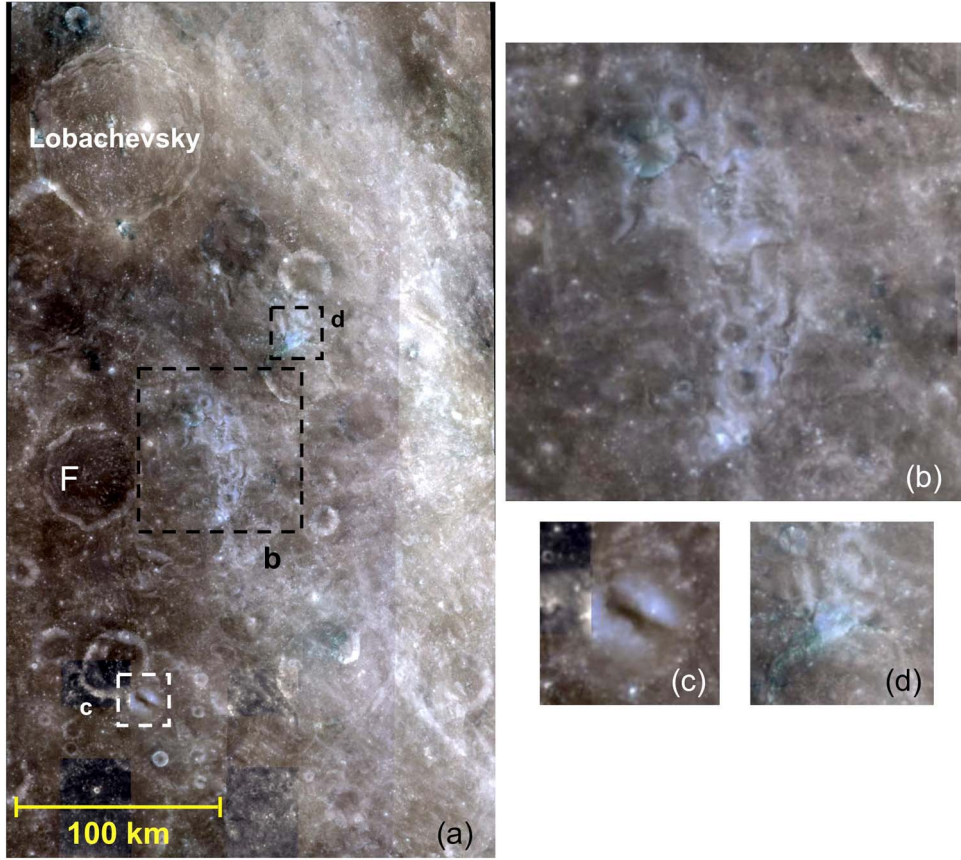


Figure 16. The Firsov swirls. Image covers 12°N – 2°S , 111°E – 119°E . RGB color assignments are as in Figure 1. Portions of the scene missing data in one of the spectral bands have been filled in with pixels from other bands. Dashed boxes labeled b, c, and d in Figure 16a indicate the areas of insets in Figures 16b, 16c, and 16d, respectively. Label F is crater Firsov (51 km diameter). (b) swirls in the Apollo 10 image of Figure 15. (c, d) High-reflectance loops with darker central lanes typical of other highland swirls, e.g., at Airy.

northern highland background has an average FeO content of 6.1 wt.%; the northwestern highland background ROI has 5.8 wt.%. The northwestern background region approximately coincides with the Apollo 16 standard telescopic observing site. The slightly lower FeO abundance of the central anomaly compared with the two highland background regions is illustrated in the NIR ratio-reflectance plot presented in Figure 23. The points for the central anomaly fall slightly to the upper right of the maturation trend for the highland background areas. The immaturity of the albedo anomaly (greater average OMAT value, Table 2) compared with the two background regions corresponds to the location of the albedo anomaly cluster at a greater distance from the origin used to define the OMAT parameter (Figure 23, compare Figure 17).

7.6. Gerasimovich

[67] The characteristics of the Gerasimovich swirl (Figure 24) revealed in the FeO and OMAT images are similar to those at Descartes, except that the Clementine FeO values for the main Gerasimovich swirl are essentially the same as those of the surroundings. The Gerasimovich main swirl clearly stands out in the OMAT image (Figure 24b). The bright swirl material has small, subtle differences from the adjacent

lower-albedo surface in the FeO image (Figure 24c). Some boundaries in the FeO image that have counterparts in the reflectance and OMAT images can be identified, but elsewhere in the FeO image the main swirl cannot be readily distinguished from the surroundings. The Gerasimovich main swirl ROI has average FeO of 5.9 wt.%, which, within the standard deviation, overlaps with the 5.7 and 5.8 wt.% averages of the two background regions (Table 2). In the NIR ratio-reflectance plot for Gerasimovich (Figure 25) the clusters of points for the three regions lie roughly on the same trend, corresponding to approximately equal θ values and hence to very similar FeO abundances according to the Lucey algorithm (compare with Figure 17). The background regions are clearly more mature (lower average OMAT) than the main swirl (Table 2).

8. Implications for the Origin of Lunar Swirls

8.1. Discussion

[68] The correlation of swirls with magnetic anomalies suggests that there is a link between these two phenomena. It has been suggested that comet impacts could impress a magnetic field on the lunar surface [Gold and Soter, 1976; Schultz and Srnka, 1980]. However, several lines of evidence

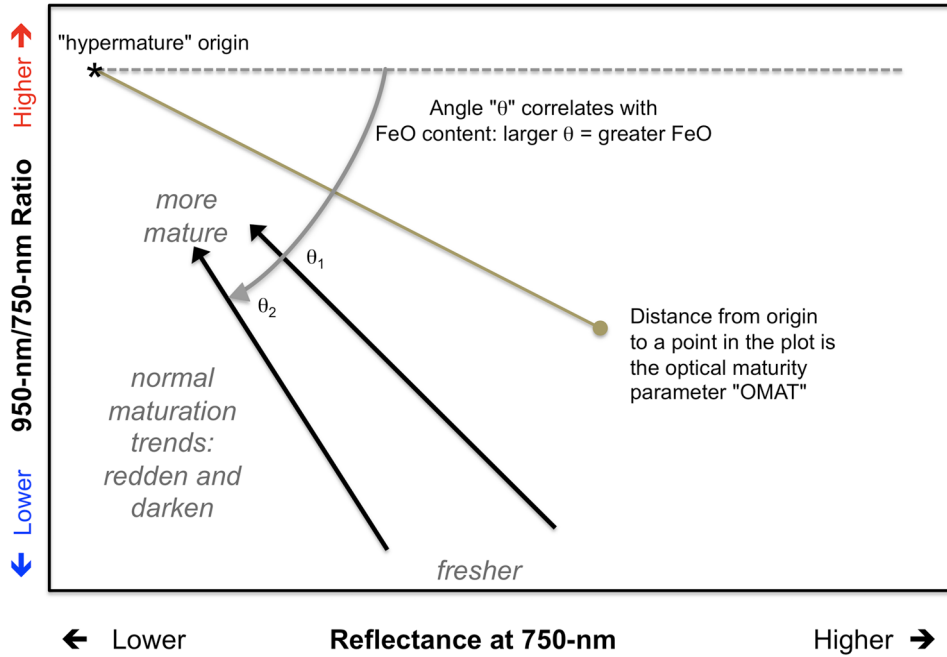


Figure 17. Conceptual NIR ratio-reflectance plot illustrating the definitions of the Lucey *et al.* [2000a, 2000b] FeO and optical maturity (OMAT) parameters. Normal space weathering proceeds from lower right (fresh material) to upper left (more mature material). Material with a particular FeO content falls along a maturity trajectory with constant θ , the spectral parameter that is highly correlated with the inherent ferrous iron content of the silicates. In the diagram, the material at θ_1 has a lower FeO content than that at θ_2 . A greater distance from the origin corresponds to a larger value of the OMAT parameter, that is, fresher material. See Lucey *et al.* [2000a, 2000b] for the exact equations used in the definition of the parameters.

argue against a comet-impact origin for swirls. First, if a thin surface layer of material was modified by the action of cometary dust and gas, it appears that the degree of magnetization required to produce the observed magnetic fields would be unrealistically high [Nicholas *et al.*, 2007]. Second, comets are predicted to strike the planet Mercury with greater frequency than they do the Moon [Gold and Soter, 1976; Starukhina and Shkuratov, 2004]. Therefore, if the comet-impact origin of lunar swirls is correct, then Mercury should exhibit swirls in even greater numbers than does the Moon. However, combined Mariner 10 and MESSENGER images are now available for nearly the entire surface of Mercury, and no example of a lunar-like swirl has been found [Blewett *et al.*, 2010a]. Further, the comet-impact model does not predict a difference in FeO content between the putative comet-scoured surface and the unmodified background terrain, contrary to the observations we describe in section 7.

[69] Thus, for the present, we set aside hypotheses for swirl formation that involve comet impacts. Older hypotheses attributed swirls to nuée ardente deposits produced by pyroclastic flows [McCauley, 1967] or to material derived from sublimation of volatiles from the lunar interior [e.g., Whitaker, 1969; El-Baz, 1972; Schultz, 1976]. These mechanisms should produce unusual compositions, which we do not observe, and do not explain the coincidence of swirls with areas of magnetized crust.

[70] Other concepts for swirl formation hinge on interaction between a preexisting magnetic anomaly and the solar wind. As mentioned above, terranes with remnant magne-

tism could have been produced by fields generated by a core dynamo early in lunar history or by deposition of magnetized basin ejecta. Two solar wind related hypotheses for the origin of lunar swirls are diminished space weathering caused by magnetic shielding of the surface from the solar wind [e.g., Hood and Schubert, 1980; Hood and Williams, 1989] and electrostatic movement and concentration of fine-grained plagioclase-rich dust [Garrick-Bethell *et al.*, 2009a, 2010]. We next describe how our multispectral Clementine observations and other evidence fit with the predictions of these two models.

8.2. Solar Wind Shielding

[71] The solar wind shielding hypothesis holds that decreased solar wind flux within a magnetic anomaly [e.g., Hood and Williams, 1989; Harnett and Winglee, 2000] is responsible for delaying or preventing the normal process of lunar space weathering (optical maturation) and thus maintaining within the swirls the spectral characteristics of unweathered material. Our findings and the work of others [Bell and Hawke, 1981, 1987] indicate that the high-reflectance portions of the swirls indeed have spectral characteristics consistent with immature material. The swirls are visible predominantly because of maturity differences with the background. Evidence for the presence of mini-magnetospheres over Reiner Gamma [Kurata *et al.*, 2005; Nicholas *et al.*, 2007] and Gerasimovich [Halekas *et al.*, 2008; Wieser *et al.*, 2010], two of the strongest magnetic anomalies, indicates that the surface in these areas is in fact

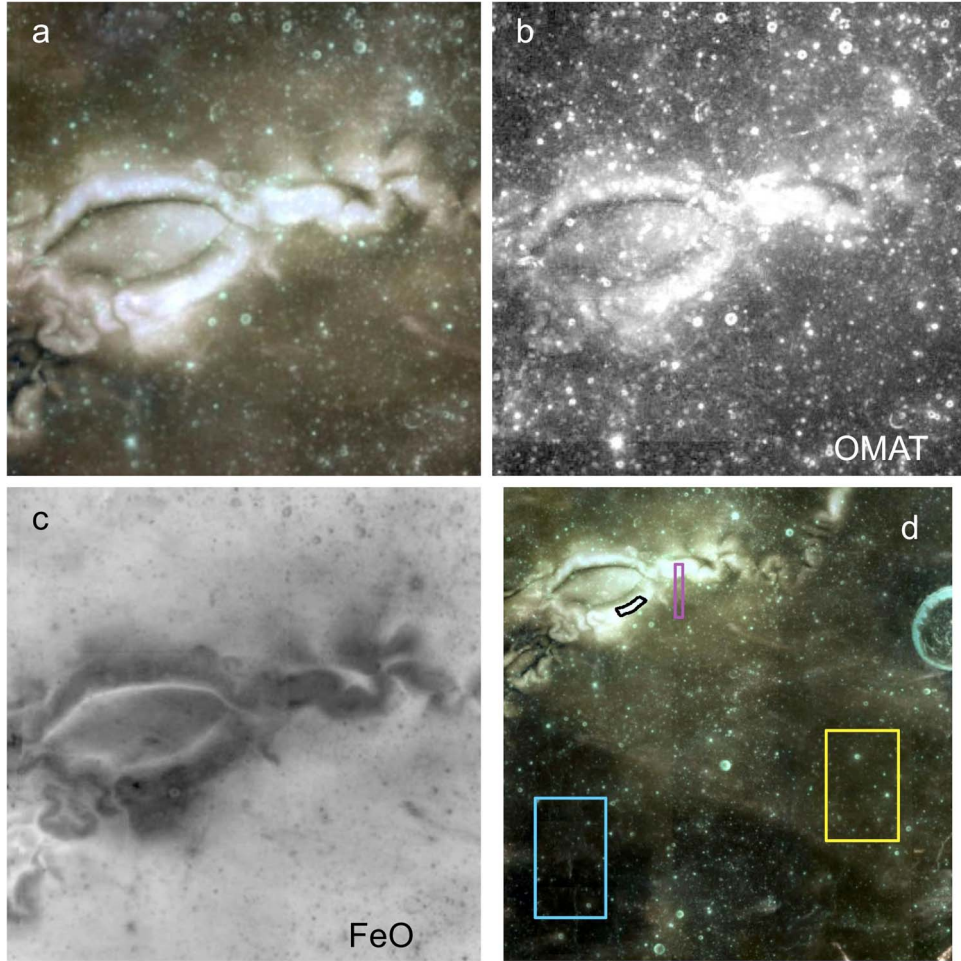


Figure 18. Reiner Gamma. (a) Clementine RGB close-up of the main swirl. (b) Optical maturity parameter (OMAT) image. Brighter tones correspond to fresher material. Linear contrast stretch is 0.14 to 0.29. (c) Ferrous iron abundance image. Brighter tones indicate greater FeO content. Linear stretch is 14.5 to 20.0 wt.% FeO. (d) Locator map for Reiner Gamma image regions-of-interest (ROIs) plotted in Figure 19. Black lines enclose a portion of the bright swirl. Yellow = mare background south 1. Cyan = mare background south 2. Magenta = transect of main swirl.

Table 2. Data for Image Regions of Interest Shown in Figures 18 to 21

Region of Interest	Avg. Wt.% FeO ^a	Avg. OMAT ^{a,b}	No. of Pixels
<i>Reiner Gamma</i>			
Bright swirl	15.7 ± 0.1	0.289 ± 0.011	589
Mare background S1	18.8 ± 0.2	0.172 ± 0.019	23312
Mare background S2	19.4 ± 0.2	0.162 ± 0.015	24805
<i>Mare Ingenii</i>			
Thom. M swirl	14.1 ± 0.4	0.242 ± 0.019	4170
Thom. M background	16.2 ± 0.2	0.163 ± 0.010	1380
<i>Descartes</i>			
Central albedo anomaly	4.5 ± 0.4	0.246 ± 0.009	4757
Background north	6.1 ± 0.7	0.152 ± 0.010	5280
Background northwest	5.8 ± 0.6	0.147 ± 0.011	8736
<i>Gerasimovich</i>			
Main swirl	5.9 ± 0.4	0.216 ± 0.010	1188
Background north	5.7 ± 0.7	0.167 ± 0.012	2256
Background southwest	5.8 ± 0.6	0.147 ± 0.011	3009

^aRange of variation is the standard deviation.

^bOptical maturity parameter.

experiencing decreased solar wind flux, a necessary prerequisite for the solar wind shielding model. Some dark lanes may be “overmatured” areas receiving enhanced solar wind flux because of scattering or focusing from the magnetically shielded areas [e.g., *Hood and Williams*, 1989].

[72] In order for the solar wind shielding hypothesis to be correct, the solar wind must necessarily be a key agent of space weathering on the Moon. For example, while a magnetic anomaly may shield the surface from the solar wind, it will not block the flux of micrometeoroids [*Richmond et al.*, 2003]. The vapor-deposited blebs and coatings of nanophase metallic iron that are responsible for the optical effects of space weathering are thought to be produced by both micrometeoroid impact and solar wind ion sputtering [e.g., *Pieters et al.*, 2000; *Hapke*, 2001]. It seems virtually certain that micrometeoroid bombardment will produce and deposit vapors in the lunar regolith (see calculations by *Hapke* [2001]). It could be that solar wind exposure is somehow a precondition for impact vaporization to reduce ferrous iron to its metallic form in the vapor deposits, but the arguments reviewed by *Hapke* [2001] and

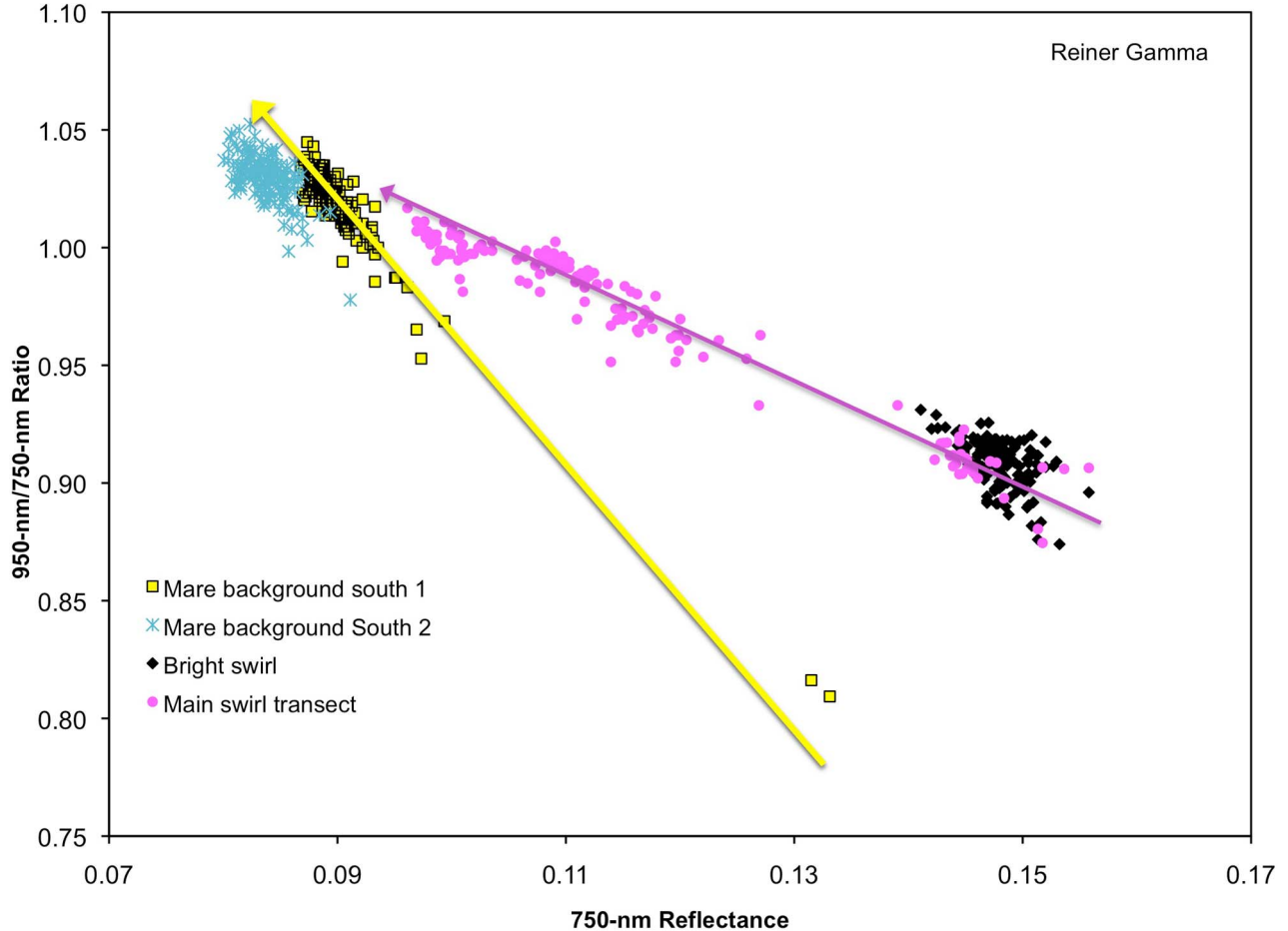


Figure 19. Ratio-reflectance scatterplot for image ROIs at the Reiner Gamma Formation. Color of plot symbols corresponds to color of lines demarcating the ROIs in Figure 18d. For each ROI, 150 randomly selected image pixels are plotted. The near-infrared ratio-reflectance diagram illustrates trends related to ferrous iron abundance and maturity. In general, material will move toward the upper left as space weathering proceeds, as indicated by the normal weathering trend of the background mare (yellow arrow). Material with higher ferrous iron abundance plots toward the lower left. Cross-cutting trend in the main swirl transect pixels (magenta points and arrow) suggests compositional mixing between swirl material and mare background. Arrows are for illustrative purposes and do not represent fits to the data.

laser pulse experiments simulating impact space weathering of powdered minerals [e.g., Yamada *et al.*, 1999; Sasaki *et al.*, 2001] suggest that darkening and reddening occur without the need for implanted hydrogen.

[73] Estimates of the timescales for weathering by the two processes (micrometeoroid impact or solar wind ion bombardment) differ substantially. Hapke [1977] estimated times of $\sim 2 \times 10^5$ years for darkening of undisturbed lunar rock powder by either solar wind sputtering or micrometeoroid impact vaporization. If this is correct, then the solar wind and micrometeoroids ought to make an equal contribution to lunar soil maturation. By contrast, from their laser irradiation experiments simulating micrometeoroid impacts, Yamada *et al.* [1999] estimated that $\sim 10^8$ years are needed at a solar distance of 1 astronomical unit to produce major optical changes. In this case, solar wind sputtering would be the dominant source of lunar space weathering (10^5 versus 10^8 years, i.e., the solar wind generates optical changes ~ 1000 times faster than does micrometeoroid impact).

Spectral study of asteroid families created by recent collisional break-up suggests that reddening of asteroid surfaces takes place rapidly ($\sim 10^6$ years) and hence favors the solar wind as the primary agent of space weathering in the asteroid belt [Vernazza *et al.*, 2009].

[74] Note that the time required for the rays of large lunar craters to reach optical maturity is considered to be $\sim 10^9$ years, based on the example of the Copernicus crater. Copernicus is thought to have an age of ~ 800 Myr, and its ray system has nearly reached full optical maturity [Grier *et al.*, 2001; Hawke *et al.*, 2004]. The longer time required for actual maturation of Copernicus' rays ($\sim 10^9$ years) relative to the estimates for maturation by solar wind sputtering (10^5 years) or micrometeoroid bombardment (10^5 or 10^8 years) can be explained by exposure of fresh material as boulders and blocks in the rays are broken down. This process on the real Moon contrasts with the undisturbed powders considered in the space-weathering time estimates.

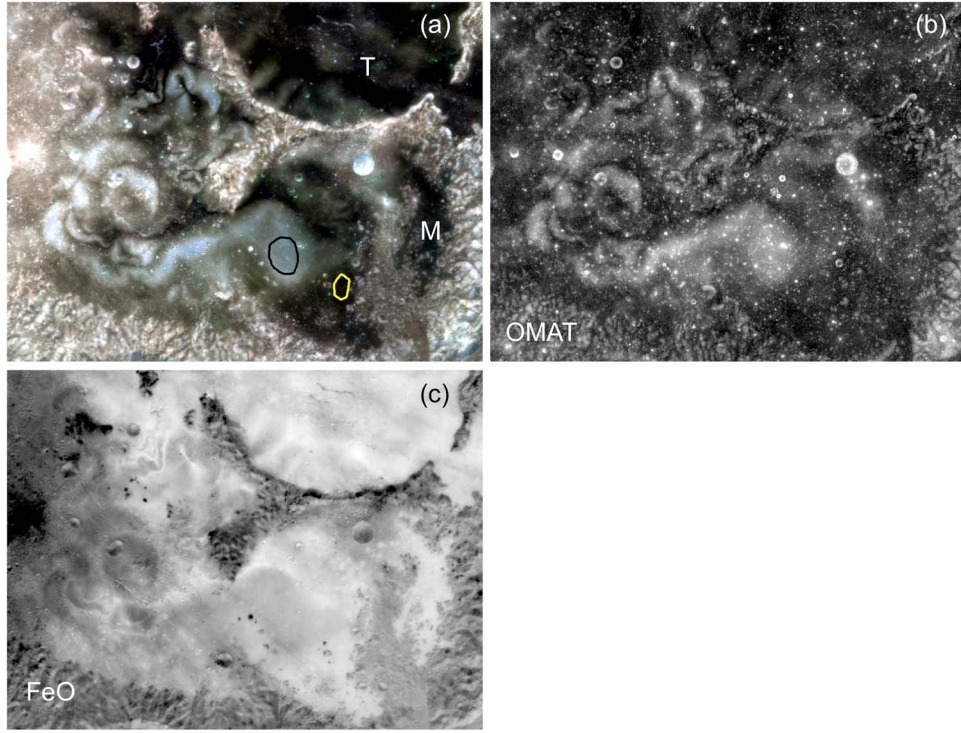


Figure 20. Mare Ingenii. (a) Clementine RGB close-up of the swirls. Label T is crater Thomson; M is Thomson M. (b) OMAT image. Brighter tones correspond to fresher material. Linear contrast stretch is 0.12 to 0.32. (c) Ferrous iron abundance image. Brighter tones indicate greater FeO content. Linear stretch is 5.5 to 18.5 wt.% FeO. Image ROIs outlined in Figure 20a are plotted in Figure 21. Black = Thomson M swirl. Yellow = Thomson M mare background.

[75] If the major magnetic anomalies were emplaced at the time of basin formation, as suggested by the antipodal correlation [Lin *et al.*, 1988; Hood *et al.*, 2001; Richmond *et al.*, 2005; Mitchell *et al.*, 2008], then the magnetic anomalies date to roughly 3.8 Gyr. Does this mean that the swirls visible today are also \sim 3.8 Gyr old? It could be that ejecta from craters outside a magnetic anomaly are occasionally deposited within the magnetically shielded area, thus “refreshing” the surface [Hood *et al.*, 1979a, 2001]. If this is the case, then the degree of solar wind shielding required to maintain the visibility of the swirl could be less than that needed in the absence of the addition of outside material. Consider this hypothetical example by way of illustration: Assume the maturation time for normal flat surfaces is 500 Myr, and that at a particular location a crustal magnetic field provides 50% shielding from the solar wind. The maturation time within the shielded area would presumably double to 1 Gyr. Therefore, ejecta deposited in the shielded area at 750 Myr could still appear fresh, while nearby nonshielded surfaces would have reached full optical maturity. If this process is in fact taking place, the refreshing of shielded surfaces by deposition of ejecta may mean that the swirls visible today do not necessarily date from the time of formation of the magnetic anomalies. Thus, according to the “solar wind shielding with ejecta refreshment” model, the age and existence of the swirls are a function of the strength and configuration of the magnetic anomaly at a particular location, and in addition have a dependence on the (stochastic) process of ejecta input. Perhaps magnetic anomalies such as

the ones at Abel, Hartwig, and Stöfler lack perceptible swirls because the area has not received sufficient recent refreshing ejecta input.

[76] Our FeO abundance maps reveal small but measurable compositional differences between most bright swirls and their surroundings, with the bright areas having lower FeO content (see sections 7.3 to 7.6). These findings for Reiner Gamma are in qualitative agreement with the approximately 5–10% highland component detected at Reiner Gamma by Bell and Hawke [1981, 1987] based on mixing model analysis of telescopic reflectance spectra in the NIR (0.6–2.5 μ m). The addition of lower-FeO ejecta material derived from highland impacts could potentially explain the compositional differences observed in the Clementine-derived FeO maps. For example, Hood *et al.* [1979a, 1979b] have discussed evidence that craters Glushko (Olbers A) or Cavalierius contributed material to Reiner Gamma. It is known that mare regolith can contain a nonnegligible highland component, for example the finding of 20% feldspathic material contained in Apollo 11 soils by Korotev and Gillis [2001].

[77] The iron-mapping algorithm of Lucey *et al.* [2000a] was developed using Clementine multispectral observations of the Apollo and Luna sample return sites, and calibrated using the laboratory-determined FeO contents of the samples returned from those sites. The Apollo and Luna sampling sites include typical fresh and mature surfaces. If abnormal space weathering is taking place within the magnetic anomalies, as postulated by the solar wind shielding concept for swirl formation, could this violate the assumptions of the

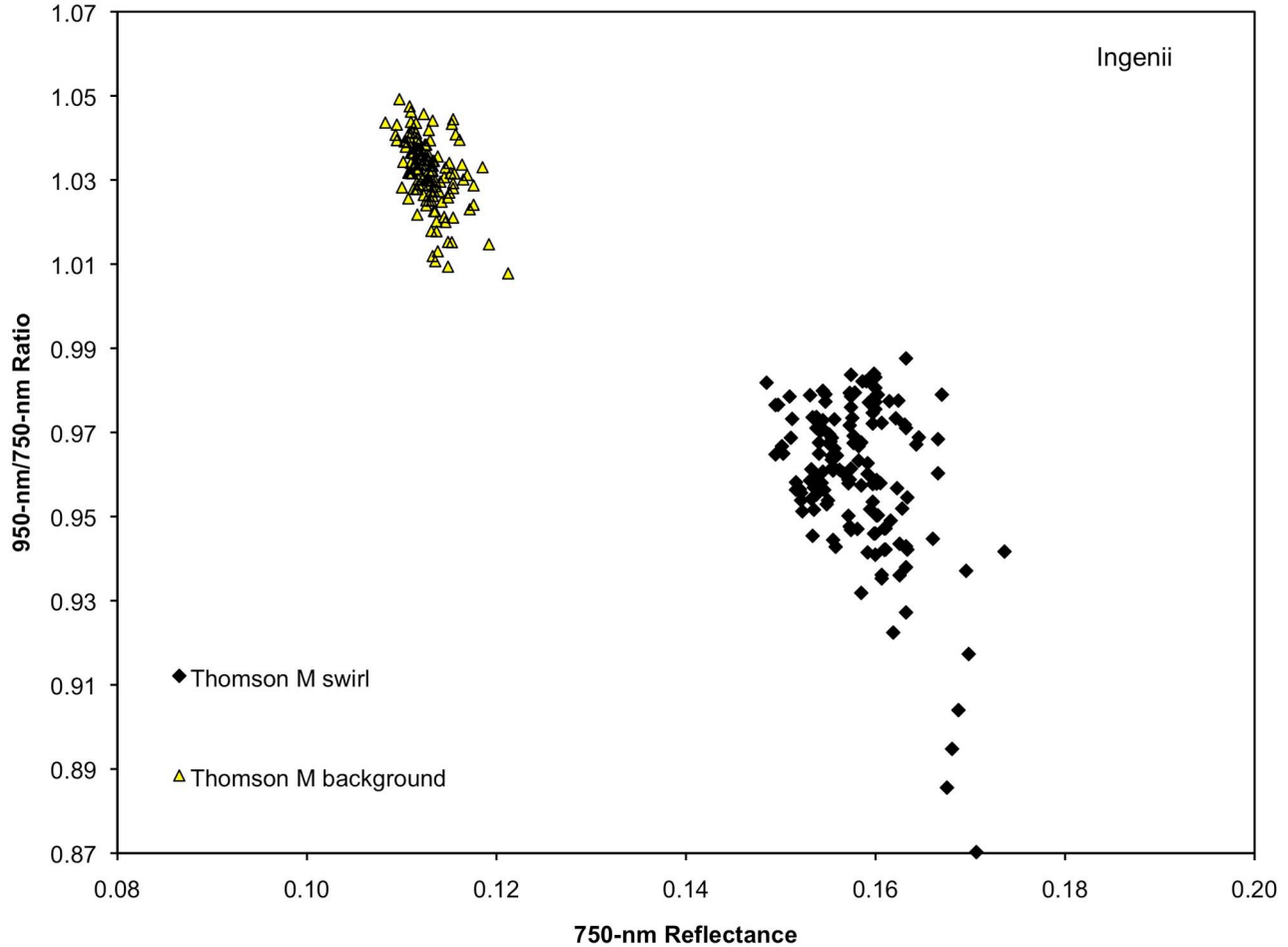


Figure 21. NIR ratio-reflectance scatterplot for image ROIs at the Mare Ingenii swirl. Color of plot symbols corresponds to color of lines outlining the ROIs in Figure 20a. For each ROI, 150 randomly selected image pixels are plotted. The swirl surface has higher reflectance and lower 950 nm/750 nm reflectance ratio than the mare background, and the swirl points lie along a different weathering trend than that defined by the background points.

Lucey algorithm and produce erroneous values? To answer this question, we consider the role of nanophase iron in producing the optical effects of space weathering. In section 7.1 we reviewed the current understanding of the way that the size of the npFe^0 particles and coatings in a soil controls the degree of reddening and darkening the soil exhibits [e.g., Hapke, 2001]. It is thought that smaller npFe^0 particles and coatings (less than ~ 10 nm) are created by vapor phase deposition during micrometeoroid impact and solar wind sputtering. Larger npFe^0 (greater than ~ 50 nm) particles form during micrometeoroid impact melting and hence are found within agglutinates. The smaller npFe^0 produce reddening and some darkening, while the larger npFe^0 are responsible mainly for overall darkening [Noble et al., 2007].

[78] Therefore, there are several possible consequences for a surface that receives reduced solar wind bombardment because of the presence of a magnetic shield. (1) Decreased solar wind sputtering might decrease the production of vapors, and hence the soil would accumulate small npFe^0 at a slower rate than normal. Thus the soil would remain brighter and unreddened longer than usual. (2a) If implanted solar wind H is needed for the reduction of FeO in minerals

and glasses to large npFe^0 grains during impact melting, then a shielded surface would not build up large npFe^0 at the normal rate and consequently would not darken as quickly. (2b) If larger-size npFe^0 is produced during melting by coalescence of the smaller npFe^0 coatings that formed by vapor phase deposition, then in a shielded surface the deficit of small npFe^0 would lead to a deficit of large npFe^0 , and hence to a lack of darkening. Presumably some small npFe^0 would still be generated by micrometeoroid impact vaporization, so the predicted optical characteristics of a surface shielded from the solar wind are that it would undergo a decreased amount of reddening and little darkening compared to the normal situation.

[79] The normal space-weathering trend includes both darkening and reddening, with trajectories that depend on the innate FeO content of the surface, as illustrated in Figure 17. Clearly the swirls have not darkened substantially. As described in the preceding paragraph, the expected weathering trend in a magnetically protected area can be thought of as “partial reddening with little darkening.” This abnormal trend is depicted in Figure 26. Rather than moving up and to the left in the NIR ratio-reflectance diagram, a

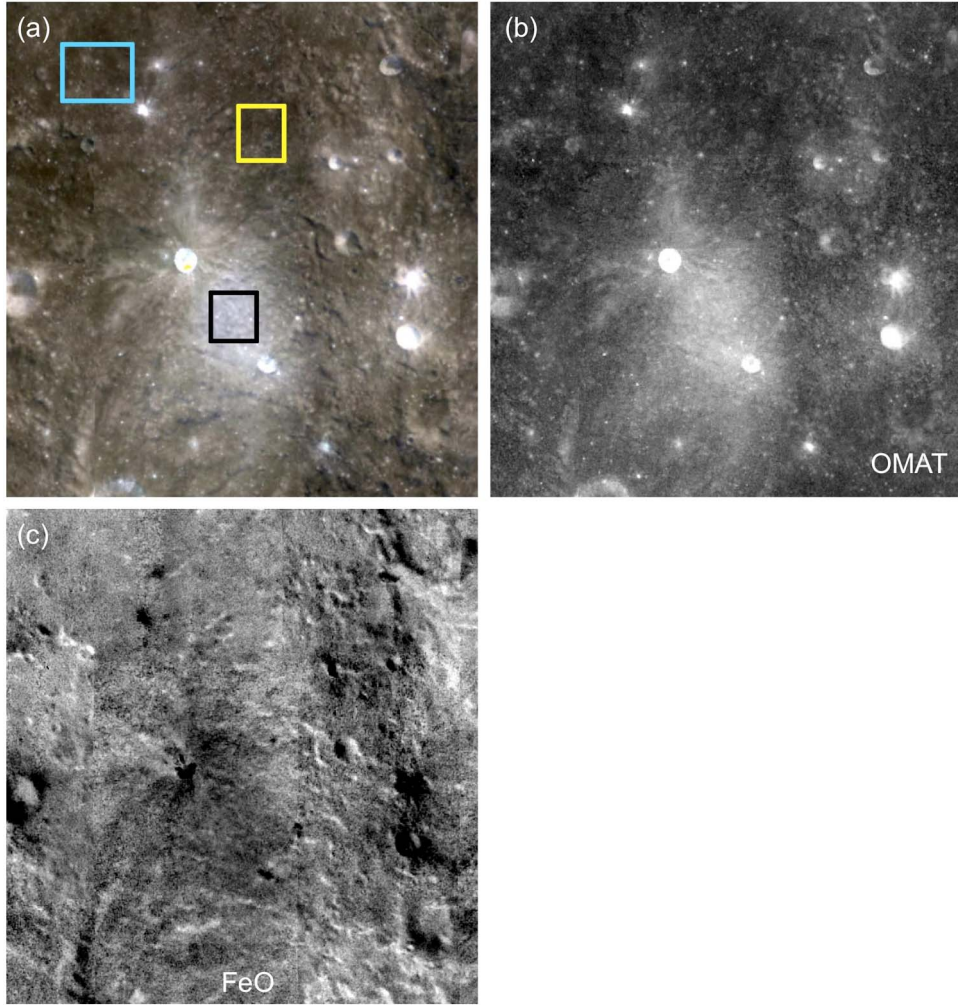


Figure 22. Descartes. (a) Clementine RGB close-up of the swirl-like albedo anomaly. (b) OMAT image. Brighter tones correspond to fresher material. Linear contrast stretch is 0.12 to 0.30. (c) Ferrous iron abundance image. Brighter tones indicate greater FeO content. Linear stretch is 3 to 9 wt.% FeO. Image ROIs outlined in Figure 22a are plotted in Figure 23. Black = central albedo anomaly. Yellow = highland background north. Cyan = highland background northwest.

shielded surface would tend to move slowly upward (to a greater 950 nm/750 nm reflectance ratio, i.e., become slightly redder) with little movement to the left (i.e., little effect on 750 nm reflectance). A result of this atypical trajectory in ratio-reflectance space is that the shielded material will move to an apparently smaller value of the angular FeO-sensitive parameter θ (see Figure 26) and hence map to a lower FeO content according to the Lucey *et al.* [2000a] algorithm. If correct, this process could therefore explain the slightly lower FeO content of the bright swirls compared to their surroundings in our Clementine FeO maps. In the maria, the normal weathering trajectories are steeper than those in the highlands (because of greater FeO content and thus larger θ). Therefore, at the mare sites, the lack of darkening attributed to magnetic shielding could lead to a relatively greater shift in θ than at the highland locations. This effect can be seen by inspection of the ratio-reflectance plots (Figures 22–25) and might explain the greater compositional contrasts (swirl versus background) seen in the mare site FeO images (Figures 18 and 20) than in the highland site

FeO images (Figures 22 and 24) and listed in Table 2. Kramer *et al.* [2010] have described size-dependent effects of npFe⁰ in the UV-visible range associated with magnetic shielding that could affect the predictions of the multispectral titanium-mapping algorithm of Lucey *et al.* [2000a].

[80] In summary, according to the solar wind shielding model, there are two possible ways to explain the observed differences in FeO content between bright swirl material and the surroundings. The first is that ejecta from a lower-FeO source were deposited within a magnetically shielded area. The second involves the actual mechanism of anomalous space weathering (lack of production of large-grained npFe⁰ and decreased production of small-grained npFe⁰) and the effects on the Clementine spectral iron parameter that lead to an apparently lower FeO content. It could be that at some locations both effects are operating.

[81] An aspect of the swirls that the solar wind shielding model may not account for is their photometric behavior. Swirls including the Reiner Gamma Formation have been shown to have anomalous photometric properties [Kreslavsky

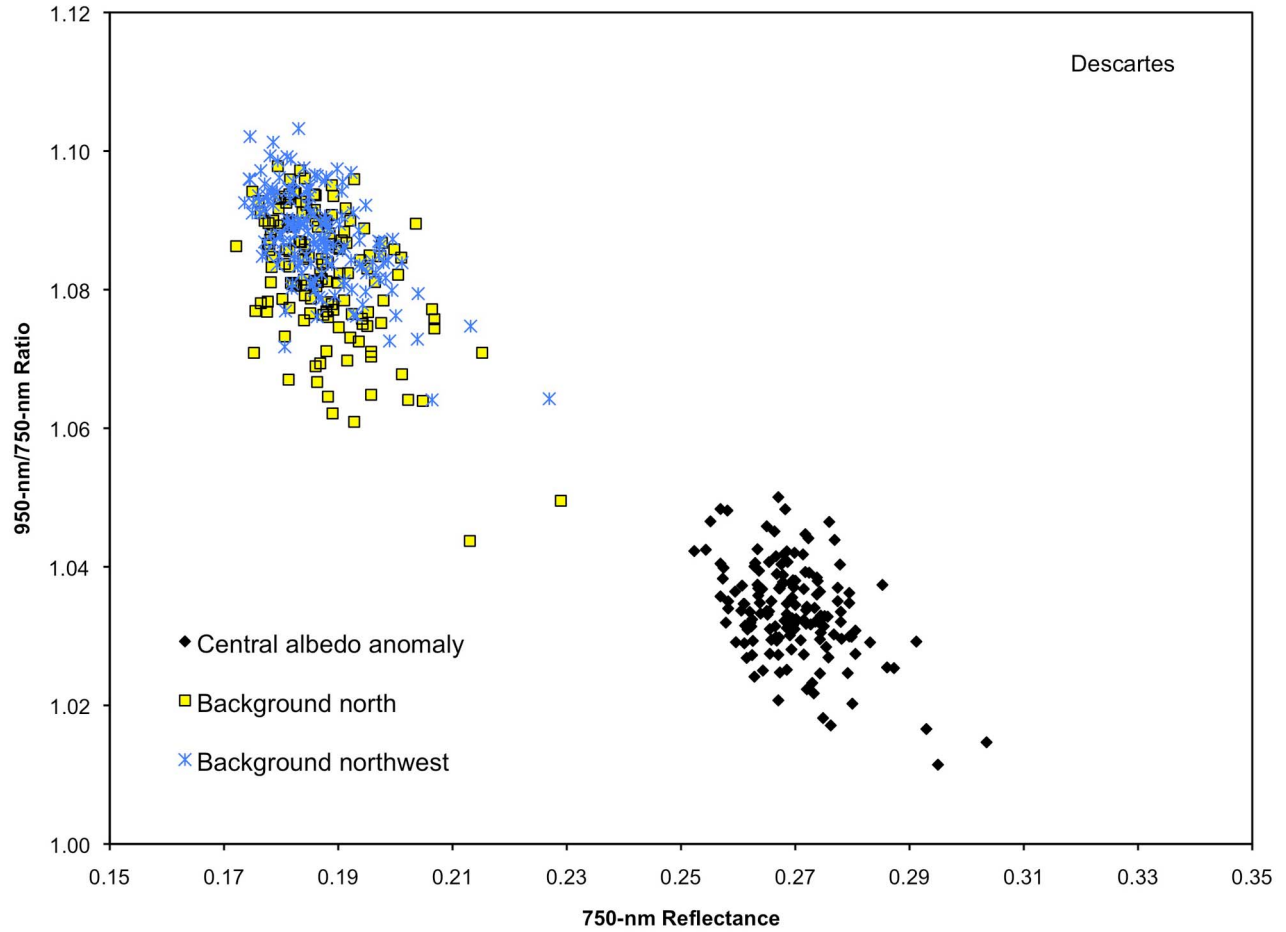


Figure 23. NIR ratio-reflectance scatterplot for image ROIs at the Descartes albedo anomaly. Color of plot symbols corresponds to color of lines outlining the ROIs in Figure 22a. For each ROI, 150 randomly selected image pixels are plotted. The location of the points for the central albedo anomaly suggests lower FeO content and lesser maturity relative to the two background regions.

et al., 2000; Kreslavsky and Shkuratov, 2003; Kaydash et al., 2009; Shkuratov et al., 2010], although the longstanding notion that Reiner Gamma is strongly forward scattering [e.g., Schultz and Srnka, 1980] has been challenged [Opanasenko and Shkuratov, 2004]. The photometric function of a regolith has generally been linked to properties including a surface's microtexture and the scattering behavior of individual soil particles (e.g., Hapke [1993]). The regolith within the magnetically shielded areas is affected by impacts of all sizes and would not be expected to differ in characteristics such as porosity or subresolution roughness from nonshielded areas. As discussed above, there are predicted differences in the size distribution of nanophase iron associated with abnormal space weathering, but detailed radiative transfer modeling would be needed in order to ascertain if a change in the size distribution of nanophase iron could alter the photometric behavior of a surface.

8.3. Electrostatic Dust Movement

[82] The electrostatic dust accumulation concept has only recently been put forward [Garrick-Bethell et al., 2009a, 2010]. It remains to be seen if the mechanism of electric field generation via separation of electrons and protons as

they penetrate to different depths in the magnetic field over a crustal magnetic anomaly is viable. Nonetheless, these electric fields are hypothesized to cause preferential accumulation of fine dust grains that were electrostatically lofted by other processes. The finest grain-size fraction (<10 μm) of lunar soil particles is enriched in plagioclase [e.g., Walker and Papike, 1981; Taylor et al., 2001] because feldspar is more readily comminuted by impacts than other common lunar minerals [Cintala and Hörz, 1992]. Here we evaluate the hypothesis in terms of the observable consequences of swirl deposits consisting of a fine-grained, plagioclase-dominated dust assemblage.

[83] Garrick-Bethell et al. [2010] presented a Clementine NIR ratio-reflectance plot for portions of the Mare Ingenii swirl, similar to our Figure 21. They identified trends interpreted as compositional mixing between bright swirl material and the background. Garrick-Bethell et al. [2010] state that the solar wind deflection model would predict only maturity-related differences, and hence conclude that evidence for compositional mixing supports their dust accumulation model. In our study of both mare and highland swirls, we find similar evidence for a low-FeO compositional component within the swirls (section 7 above), evident in our visible and

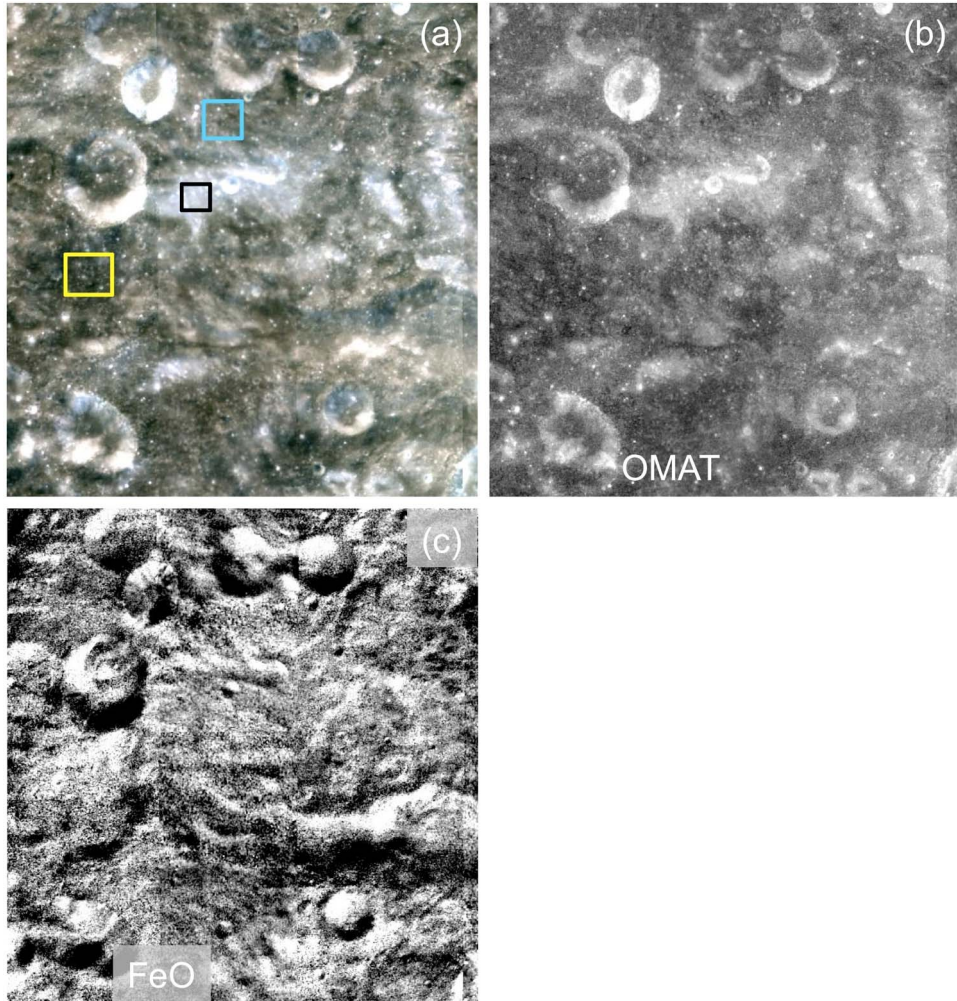


Figure 24. Gerasimovich. (a) Clementine RGB close-up of the high-reflectance albedo anomaly. (b) OMAT image. Brighter tones correspond to fresher material. Linear contrast stretch is 0.11 to 0.25. (c) Ferrous iron abundance image. Brighter tones indicate greater FeO content. Linear stretch is 4.5 to 7 wt.% FeO. Image ROIs outlined in Figure 24a are plotted in Figure 25. Black = main swirl. Yellow = highland background southwest. Cyan = highland background north.

NIR ratio-reflectance plots and in the FeO images. However, in section 8.2 we have discussed two reasons that could, within the solar wind shielding model, account for the apparent relatively low FeO content of the swirls.

[84] The electrostatic dust accumulation concept does offer an alternative explanation for the observed high reflectance of the swirls and their apparently low FeO content relative to the surroundings as judged from the relationships exhibited in the NIR ratio-reflectance plots. The putative dust deposits, being preferentially enriched in plagioclase, would be expected to have lower ferrous iron content than nearby normal surfaces. Our observation that the compositional contrast between bright swirl and surroundings is greater for mare swirls than for highland swirls could also be explained if the swirls are dominated by feldspar-rich dust. This is because plagioclase is the chief rock-forming mineral in the highlands, and highland rocks have a lower abundance of iron-bearing pyroxenes or olivines than found in mare basalts. Therefore a process that concentrated plagioclase dust grains at the optical surface would produce less com-

positional contrast in the highlands than it would in the maria. In addition, it is reasonable to expect that deposits of dust would have anomalous photometric properties, as is observed. This is because the process proposed to emplace the dust deposits (electrostatic lofting, settling, and concentration of the finest grains) differs from the impact bombardment and mixing that forms the normal surface of the Moon. The dust accumulations may thus have higher porosity and enhanced “fairy castle structure” [Hapke and Van Horn, 1963] compared with typical regolith; these characteristics would be predicted to cause differences in texture and hence in photometric behavior.

[85] Several remote-sensing techniques can provide information on grain size of the lunar regolith. Radar backscatter gives clues to the abundance of scatters of the size of the radar wavelength. Maps of the Reiner Gamma formation at 3.8 cm [Zisk et al., 1974] show no features that correspond to the optical swirl, and recent mapping of selected swirls at a 12 cm wavelength by the Mini-RF instrument on the Lunar Reconnaissance Orbiter spacecraft does not clearly reveal any

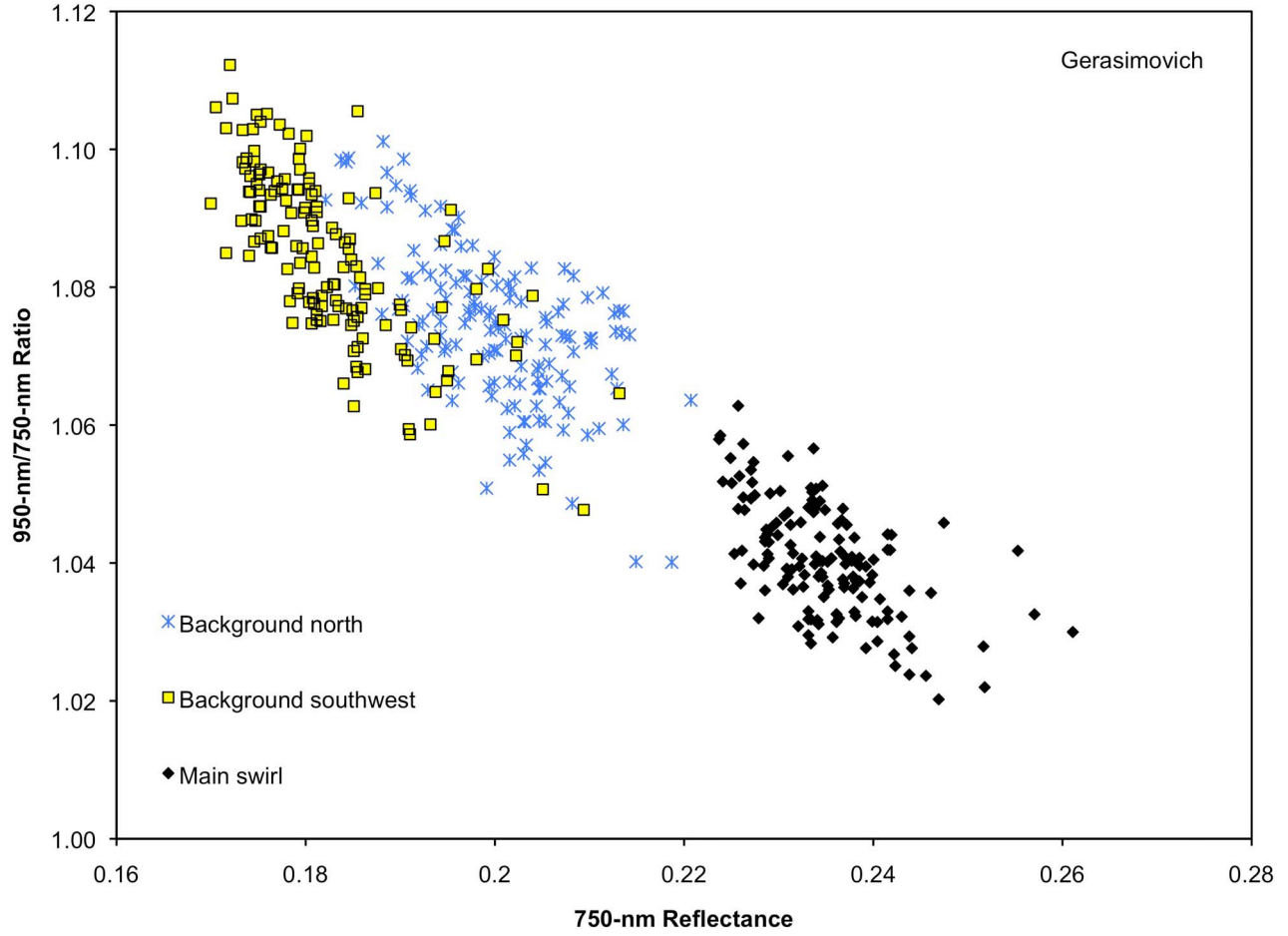


Figure 25. NIR ratio-reflectance scatterplot for image ROIs at the Gerasimovich swirl. Color of plot symbols corresponds to color of lines outlining the ROIs in Figure 20a. For each ROI, 150 randomly selected image pixels are plotted. The swirl and background points fall along approximately the same weathering path, consistent with each area having nearly the same FeO content.

difference in wavelength-scale roughness between the bright swirls and nearby background [Neish *et al.*, 2010; see also Campbell *et al.*, 2006]. This suggests that swirls have about the same abundance of centimeter-to-decimeter size rocks at the surface and in the near-subsurface as the nearby mare.

[86] Earth-based infrared measurements of temperatures during lunar eclipse [Shorthill, 1973] show an area of lower temperature that apparently corresponds to Reiner Gamma [Schultz and Srnka, 1980]. Low eclipse temperature could be caused by low thermal inertia, consistent with a fine-grained, insulating surface that cools rapidly when the Moon enters the Earth's shadow. On the other hand, a higher-albedo surface, such as a swirl, would be expected to have a lower radiative-equilibrium temperature, and hence might appear cooler than the surroundings during eclipse. However, if low thermal inertia is confirmed by data from the Diviner radiometer instrument [Paige *et al.*, 2009] onboard the Lunar Reconnaissance Orbiter spacecraft, such evidence for the presence of finer than average material at Reiner Gamma and other swirls would provide support for the existence of accumulated dust deposits. A means by which diminished solar wind flux caused by magnetic shielding could affect a bulk regolith property like thermal inertia is not readily apparent.

[87] Polarimetric, photometric, and spectral analysis can also potentially provide information on the grain size of the lunar surface, though interpretations have been difficult. Shkuratov *et al.* [2007, 2008] performed optical polarimetry of Reiner Gamma and concluded that there is a high concentration of dust in the swirl compared with the surroundings. On the other hand, photometric parameter images for Reiner Gamma have been interpreted to mean that the swirl has larger, immature particles and a greater degree of sub-resolution roughness than the surroundings [Shkuratov *et al.*, 2010]. An interpretation of larger grains was also made by Pinet *et al.* [2000], who concluded from spectral analysis that smaller grains from the main Reiner Gamma swirl had been swept away and deposited in the southwest tail region. Therefore the analysis of grain size using these techniques has produced inconsistent results and at present cannot help to distinguish among the competing hypotheses for swirl formation.

9. Conclusions

[88] We have conducted a comprehensive survey of lunar swirls and crustal magnetic anomalies. We find that all

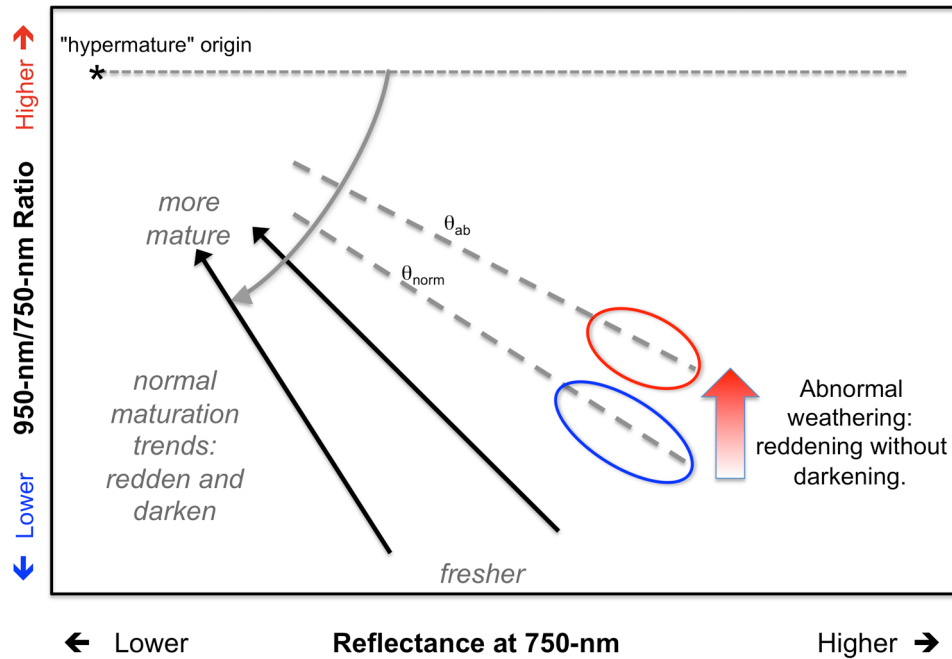


Figure 26. Conceptual NIR ratio-reflectance plot illustrating the abnormal weathering trend attributed to solar wind shielding of the surface, and the effect on the apparent FeO content as measured by the Lucey *et al.* [2000a] spectral ferrous iron parameter (compare with Figure 17). Normal surfaces mature by moving to the upper left, along constant θ trajectories, where θ is highly correlated to the FeO content. However, magnetically shielded material could undergo abnormal weathering (limited reddening with very little darkening), corresponding to predominantly vertical movement in the spectral space (i.e., from the blue oval to the red oval). This results in a smaller θ , which translates to an apparently lower FeO content.

swirls and swirl-like albedo anomalies are associated with areas of magnetized crust. Several weak or moderate magnetic anomalies (Abel, Crozier, Hartwig, and Stöfler) lack unusual albedo markings. The swirls we examined (Airy, Descartes, Firsov, Gerasimovich, Hopmann, Mare Ingenii, Mare Marginis, Mare Moscovense, north of Rima Sirsalis, northwest of Apollo basin, and Reiner Gamma) all stand out from their surroundings in images of the Lucey *et al.* [2000b] optical maturity parameter. This indicates that the high-reflectance portions of the swirls have spectral characteristics like that of relatively fresh (immature) material.

[89] Images of the multispectral ferrous iron parameter [Lucey *et al.*, 2000a] reveal small contrasts between the high-reflectance swirls and the background surface. At mare swirl locations, the swirls are well defined in the ferrous iron maps, with FeO contents that are several weight percent lower than the surroundings. Highland swirls show less structure in the FeO maps, though high-reflectance areas typically have ~0–2 wt.% lower FeO than the background. These compositional and optical maturity trends are also evident in NIR ratio-reflectance plots of image pixels for swirls and nearby surfaces.

[90] Both the solar wind shielding model and the electrostatic dust accumulation model for the origin of the lunar swirls offer explanations for the apparent low FeO content of the swirls as interpreted in NIR ratio-reflectance plots and in maps of FeO abundance made with the algorithm of Lucey *et al.* [2000a]. We have described how the relatively low FeO content of swirls as gauged by the multispectral

iron-mapping method could be a result of shifts in npFe⁰ particle size distribution caused by anomalous space weathering rather than true compositional contrasts. However, both the dust accumulation model and the “ejecta refreshment” variant of the solar wind shielding model of swirl formation predict true compositional differences. The dust accumulation concept may offer more ready explanations for the anomalous photometric characteristics and eclipse temperature reported for the Reiner Gamma swirl. However, the lack of swirls at certain crustal magnetic anomalies could be attributed to a lack of ejecta refreshment within areas protected from the solar wind.

[91] In this paper we have presented qualitative descriptions of the spectral effects of anomalous space weathering. Future studies could perform detailed modeling of swirl and background spectra using the space-weathering model of Hapke [2001] and Lucey [2010] to account for the effects of nanophase iron of different size regimes. The analysis methods employed in this report consider only the NIR ratio and reflectance at 750 nm. In future work, it will be important to evaluate the full spectral character, including the slope in the UV-visible spectrum, and the depth, width, and location of the 1 μm ferrous iron band when making comparisons between swirl and nonswirl material. This could be accomplished with Earth-based telescopic spectra, spectra from the Kaguya Spectral Profiler, or hyperspectral imaging data from the Moon Mineralogy Mapper instrument.

[92] Information on the nature of lunar swirls continues to emerge, but definitive conclusions about the origin of

swirls cannot yet be drawn. We currently favor hypotheses for swirl formation that involve the influence of a crustal magnetic anomaly on the solar wind [cf., Blewett et al., 2010a]. Key questions concerning lunar swirls and crustal magnetic anomalies that need to be answered include the following: (1) Are the crustal magnetic anomalies truly capable of causing an important decrease in the solar wind flux reaching the surface? (2) Are electric fields induced by solar wind interaction with a magnetic anomaly able to cause net accumulations of fine dust? (3) Can crustal magnetic anomalies be used to disentangle the effects of space weathering caused by solar wind sputtering from those due to micrometeorite bombardment? (4) Do prominent swirls in areas of lower magnetic field intensity actually have small-scale strong fields at the surface that are below the spatial resolution of available orbital measurements? (5) To what extent does input of younger crater ejecta from outside a swirl contribute to the swirl's visibility? (6) Can the absence of high-albedo swirl markings at some weak- and moderate-strength magnetic anomalies be explained by a lack of timely refreshment by ejecta deposition? (7) Can measurements independent of the multispectral iron-mapping algorithm confirm the existence of compositional differences between swirl material and nearby background? (8) Do swirls have a different grain size distribution than areas of normal regolith?

[93] A wealth of new data from the Kaguya, Chandrayaan-1, Chang'E-1, and Lunar Reconnaissance Orbiter spacecraft is becoming available, and this will lead to further progress in our understanding of the lunar swirls. Ultimately, in situ exploration may be needed to fully solve the puzzle of swirl origin. As advocated by Richmond and Hood [2008b] and Blewett et al. [2010b], a rover or lander targeted to a prominent albedo and magnetic anomaly and carrying a magnetometer, solar wind spectrometer, Mössbauer spectrometer, X-ray diffraction instrument, UV-visible NIR spectrometer, and a microscopic imager would provide important information on the nature of swirls, the source of magnetic anomalies, and the role of the solar wind in space weathering.

[94] **Acknowledgments.** This work made use of the "gridview" data manipulation tool, developed by Jim Roark at NASA Goddard. We thank Chuck Wood for running the LPOD website. Apollo and Lunar Orbiter images were obtained from the Lunar and Planetary Institute web repository. Clementine image cubes were retrieved from the U.S. Geological Survey's Map-A-Planet website. We thank Nicola Richmond for contributions to an earlier phase of this work. Financial support from the NASA Planetary Geology and Geophysics program is gratefully acknowledged (grants NNX08AL53G and NNX09AQ06G to D.T.B.). We appreciate the thorough reviews by Lon Hood and Sarah Noble, which helped us to make major improvements to this paper. This is HIGP publication 1872 and SOEST contribution 8025.

References

- Anderson, K. A., R. P. Lin, R. E. McGuire, J. E. McCoy, C. T. Russell, and P. J. Coleman Jr. (1977), Linear magnetization feature associated with Rima Sirsalis, *Earth Planet. Sci. Lett.*, **34**, 141–151.
- Bell, J. F., and B. R. Hawke (1981), The Reiner Gamma formation: Composition and origin as derived from remote sensing observations, *Proc. Lunar Planet. Sci. Conf. 12th*, 679–694.
- Bell, J. F., and B. R. Hawke (1987), Recent comet impacts on the moon: The evidence from remote sensing studies, *Publ. Astron. Soc. Pacific*, **99**, 862–867.
- Blewett, D. T., P. G. Lucey, B. R. Hawke, and B. L. Jolliff (1997), Clementine images of the lunar sample return stations: Refinement of FeO and TiO₂ mapping techniques, *J. Geophys. Res.*, **102**, 16,319–16,325, doi:10.1029/97JE01505.
- Blewett, D. T., B. R. Hawke, and P. G. Lucey (2005), Lunar optical maturity investigations: A possible recent impact crater and a magnetic anomaly, *J. Geophys. Res.*, **110**, E04015, doi:10.1029/2004JE002380.
- Blewett, D. T., B. R. Hawke, P. G. Lucey, and M. S. Robinson (2007a), A Mariner 10 color study of Mercurian craters, *J. Geophys. Res.*, **112**, E02005, doi:10.1029/2006JE002713.
- Blewett, D. T., B. R. Hawke, N. C. Richmond, and C. G. Hughes (2007b), A magnetic anomaly associated with an albedo feature near Airy crater in the lunar nearside highlands, *Geophys. Res. Lett.*, **34**, L24206, doi:10.1029/2007GL031670.
- Blewett, D. T., C. G. Hughes, B. R. Hawke, and N. C. Richmond (2007c), Varieties of lunar swirls, *Lunar Planet. Sci.*, **XXXVIII**, Abstract 1232.
- Blewett, D. T., M. S. Robinson, B. W. Denevi, J. J. Gillis-Davis, J. W. Head, S. C. Solomon, G. M. Holsclaw, and W. E. McClintock (2009), Multispectral images of Mercury from the first MESSENGER flyby: Analysis of global and regional color trends, *Earth Planet. Sci. Lett.*, **285**, 272–282.
- Blewett, D. T., B. W. Denevi, M. S. Robinson, C. M. Ernst, M. E. Purucker, and S. C. Solomon (2010a), The apparent lack of lunar-like swirls on Mercury: Implications for the formation of lunar swirls and for the agent of space weathering, *Icarus*, **209**, 239–246.
- Blewett, D. T., G. C. Ho, H. Korth, L. L. Hood, and J. Halekas (2010b), A landed experiment package for investigation of lunar magnetic and albedo anomalies, *Ground-based Geophysics on the Moon*, Abstract 3009, Lunar Planet. Inst., Houston, Tex.
- Campbell, B. A., L. M. Carter, D. B. Campbell, B. R. Hawke, R. R. Ghent, and J. L. Margot (2006), 20 m resolution radar studies of the Aristarchus plateau and Reiner Gamma formation, *Lunar Planet. Sci.*, **XXXVII**, Abstract 1717.
- Cintala, M. J., and F. Hörz (1992), An experimental evaluation of mineral-specific comminution, *Meteoritics*, **27**, 395–403.
- Coleman, P. J., Jr., G. Schubert, G. T. Russell, and L. R. Sharp (1972), Satellite measurements of the Moon's magnetic field: A preliminary report, *Moon*, **4**, 419–429.
- Craddock, R. A., M. S. Robinson, B. R. Hawke, and A. S. McEwen (1997), Clementine-based geology of the Moscovia basin, lunar farside, *Lunar Planet. Sci.*, **XXVIII**, Abstract 1499.
- Crawford, D. A., and P. H. Schultz (1999), Electromagnetic properties of impact generated plasma, vapor, and debris, *Int. J. Impact Eng.*, **23**, 169–180.
- El-Baz, F. (1972), The Alhazen to Abul Wafa swirl belt: An extensive field of light-colored, sinuous markings, *Apollo 16 Prelim. Sci. Rep.*, *NASA SP-315*, 29–93–29–97.
- Eliason, E. M., et al. (1999), Digital processing for a global multispectral map of the Moon from the Clementine UVVIS imaging instrument, *Lunar Planet. Sci.*, **XXX**, Abstract 1933.
- Garrick-Bethell, I., J. W. Head, and C. M. Pieters (2009a), Near-surface magnetic fields and dust transport at lunar swirls, *Eos Trans. AGU*, **90**(52), Fall Meet. Suppl., Abstract GP34A-04.
- Garrick-Bethell, I., B. P. Weiss, D. L. Shuster, and J. Buz (2009b), Early lunar magnetism, *Science*, **323**, 356–359.
- Garrick-Bethell, I., J. W. Head, and C. M. Pieters (2010), Spectral properties of lunar swirls and their formation by dust transport, *Lunar Planet. Sci. Conf. 41st*, Abstract 2675.
- Gillis, J. J., and P. D. Spudis (1996), The composition and geologic setting of lunar far side maria, *Lunar Planet. Sci.*, **XVII**, 413–414.
- Gillis, J. J., and P. D. Spudis (2000), Geology of the Smythii and Marginis region of the Moon: Using integrated remotely sensed data, *J. Geophys. Res.*, **105**, 4217–4233, doi:10.1029/1999JE001111.
- Gold, T., and S. Soter (1976), Cometary impact and the magnetization of the Moon, *Planet. Space Sci.*, **24**, 45–54.
- Grier, J. A., A. S. McEwen, P. G. Lucey, M. Milazzo, and R. G. Strom (2001), Optical maturity of ejecta from large rayed lunar craters, *J. Geophys. Res.*, **106**, 32,847–32,862, doi:10.1029/1999JE001160.
- Halekas, J. S., D. L. Mitchell, R. P. Lin, S. Frey, L. L. Hood, M. H. Acuna, and A. B. Binder (2001), Mapping of crustal magnetic anomalies on the lunar near side by the Lunar Prospector electron reflectometer, *J. Geophys. Res.*, **106**, 27,841–27,852, doi:10.1029/2000JE001380.
- Halekas, J. S., D. L. Mitchell, R. P. Lin, L. L. Hood, M. H. Acuna, and A. B. Binder (2002), Demagnetization signatures of lunar impact craters, *Geophys. Res. Lett.*, **29**(13), 1645, doi:10.1029/2001GL013924.
- Halekas, J. S., R. P. Lin, and D. L. Mitchell (2003), Magnetic fields of lunar multi-ring impact basins, *Meteorit. Planet. Sci.*, **38**, 565–578.
- Halekas, J. S., G. T. Delory, D. A. Brain, R. P. Lin, and D. L. Mitchell (2008), Density cavity observed over a strong lunar crustal magnetic anomaly in the solar wind: A minimagnetosphere?, *Planet. Space Sci.*, **56**, 941–946.
- Halekas, J. S., R. J. Lillis, R. P. Lin, M. Manga, M. E. Purucker, and R. A. Carley (2010), How strong are lunar crustal magnetic fields at

- the surface?: Considerations from a reexamination of the electron reflectometry technique, *J. Geophys. Res.*, **115**, E03006, doi:10.1029/2009JE003516.
- Hapke, B. (1977), Interpretations of optical observations of Mercury and the Moon, *Phys. Earth Planet. Inter.*, **15**, 264–274.
- Hapke, B. (1993), *Theory of Reflectance and Emittance Spectroscopy*, 450 pp., Cambridge Univ. Press, Cambridge, U. K.
- Hapke, B. (2001), Space weathering from Mercury to the asteroid belt, *J. Geophys. Res.*, **106**(E5), 10,039–10,073, doi:10.1029/2000JE001338.
- Hapke, B., and H. Van Horn (1963), Photometric studies of complex surfaces, with applications to the Moon, *J. Geophys. Res.*, **68**, 4545–4570.
- Hapke, B., G. E. Danielson Jr., K. Klaasen, and L. Wilson (1975), Photometric observations of Mercury from Mariner 10, *J. Geophys. Res.*, **80**, 2431–2443.
- Harnett, E., and R. Winglee (2000), Two-dimensional MHD simulation of the solar wind interaction with magnetic field anomalies on the surface of the Moon, *J. Geophys. Res.*, **105**, 24,997–25,007, doi:10.1029/2000JA000074.
- Hawke, B. R., D. T. Blewett, P. G. Lucey, G. A. Smith, J. F. Bell III, B. A. Campbell, and M. S. Robinson (2004), The origin of lunar crater rays, *Icarus*, **170**, 1–16.
- Head, J. W., and A. F. H. Goetz (1972), Descartes region: Evidence for Copernican-age volcanism, *J. Geophys. Res.*, **77**, 1368–1374, doi:10.1029/JB077i008p01368.
- Hodges, C. A. (1973), Geologic map of the Langrenus quadrangle of the Moon, *U.S. Geol. Surv. Misc. Geol. Invest. Map*, I-822.
- Holt, H. E. (1974), Geologic map of the Purbuck quadrangle of the Moon, *U.S. Geol. Surv. Misc. Geol. Invest. Map*, I-739.
- Hood, L. L. (1980), Bulk magnetization properties of the Fra Mauro and Reiner Gamma Formations, *Proc. Lunar Planet. Sci. Conf.* **11th**, 1879–1896.
- Hood, L. L. (1981), Sources of lunar magnetic anomalies and their bulk directions of magnetization: Additional evidence from Apollo orbital data, *Proc. Lunar Planet. Sci. Conf.* **12th**, 817–830.
- Hood, L. L. (1995), Frozen fields, *Earth Moon Planets*, **67**, 131–142.
- Hood, L. L. (2010), Central magnetic anomalies of Nectarian-aged lunar impact basins: Possible evidence for an early core dynamo, *Icarus*, doi:10.1016/j.icarus.2010.08.012, in press.
- Hood, L. L., and A. Artemieva (2008), Antipodal effects of lunar basin-forming impacts: Initial 3D simulations and comparisons with observations, *Icarus*, **193**, 485–502.
- Hood, L. L., and A. Vickery (1984), Generation of transient magnetic fields in hypervelocity meteoroid impacts with application to lunar paleomagnetism, *Proc. Lunar Planet. Sci. Conf.* **15th**, Part 1, *J. Geophys. Res.*, **89**, suppl., C211–C223.
- Hood, L. L., and C. Williams (1989), The lunar swirls: Distribution and possible origins, *Proc. Lunar Planet. Sci. Conf.* **19th**, 99–113.
- Hood, L. L., and G. Schubert (1980), Lunar magnetic anomalies and surface optical properties, *Science*, **208**, 49–51.
- Hood, L. L., and Z. Huang (1991), Formation of magnetic anomalies antipodal to lunar impact basins: Two-dimensional model calculations, *J. Geophys. Res.*, **96**, 9837–9846, doi:10.1029/91JB00308.
- Hood, L. L., P. J. Coleman Jr., and D. E. Wilhelms (1979a), Lunar nearside magnetic anomalies, *Proc. Lunar Planet. Sci. Conf.* **10th**, 2235–2257.
- Hood, L. L., P. J. Coleman Jr., and D. E. Wilhelms (1979b), The Moon: Sources of the crustal magnetic anomalies, *Science*, **204**, 53–57.
- Hood, L. L., C. T. Russell, and P. J. Coleman Jr. (1981), Contour maps of lunar remanent magnetic fields, *J. Geophys. Res.*, **86**, 1055–1069, doi:10.1029/JB086iB02p01055.
- Hood, L. L., A. Zakharian, J. Halekas, D. L. Mitchell, R. P. Lin, M. H. Acuna, and A. B. Binder (2001), Initial mapping and interpretation of lunar crustal magnetic anomalies using Lunar Prospector magnetometer data, *J. Geophys. Res.*, **106**, 27,825–27,839, doi:10.1029/2000JE001366.
- Hughes, C. G., D. T. Blewett, B. R. Hawke, and N. C. Richmond (2006), Optical maturity and magnetic studies of lunar swirls, *Lunar Planet. Sci. Conf.* **37th**, Abstract 1230.
- Isbell, C. E., E. M. Eliason, K. C. Adams, T. L. Becker, A. L. Bennett, E. M. Lee, A. S. McEwen, M. S. Robinson, J. R. Shinaman, and L. A. Weller (1999), Clementine: A multispectral digital image model archive of the Moon, *Lunar Planet. Sci.*, **XXX**, Abstract 1812.
- Kaydash, V., M. Kreslavsky, Y. Shkuratov, S. Gerasimenko, P. Pinet, J. L. Josset, S. Beauvivre, B. Foing, and the AMIE SMART-1 Team (2009), Photometric anomalies of the lunar surface studied with SMART-1 AMIE data, *Icarus*, **202**, 393–413.
- Keller, L. P., and D. S. McKay (1993), Discovery of vapor deposits in the lunar regolith, *Science*, **261**, 1305–1307.
- Korotev, R. L., and J. J. Gillis (2001), A new look at the Apollo 11 regolith and KREEP, *J. Geophys. Res.*, **106**(E6), 12,339–12,354.
- Kramer, G., J.-P. Combe, T. McCord, E. Harnett, B. R. Hawke, and D. Blewett (2010), An investigation into the effects of the magnetic anomaly on regional space weathering at Mare Ingenii and its influence on the spectra of the basalts and lunar swirls, *Lunar Planet. Sci. Conf.* **41st**, Abstract 2594.
- Kreslavsky, M. A., and Y. G. Shkuratov (2003), Photometric anomalies of the lunar surface: Results from Clementine data, *J. Geophys. Res.*, **108**(E3), 5015, doi:10.1029/2002JE001937.
- Kreslavsky, M. A., Y. G. Shkuratov, Y. I. Velikovsky, V. G. Kaydash, D. G. Stankevich, and C. M. Pieters (2000), Photometric properties of the lunar surface derived from Clementine observations, *J. Geophys. Res.*, **105**, 20,281–20,295, doi:10.1029/1999JE001150.
- Kurata, M., H. Tsunakawa, Y. Saito, H. Shibuya, M. Matsushima, and H. Shimizu (2005), Minimagnetosphere over the Reiner Gamma magnetic anomaly region on the Moon, *Geophys. Res. Lett.*, **32**, L24205, doi:10.1029/2005GL024097.
- Lin, R. P., K. A. Anderson, and L. L. Hood (1988), Lunar surface magnetic field concentrations antipodal to young large impact basins, *Icarus*, **74**, 529–541.
- Lucey, P. G. (2010), Nanophase iron that darkens but does not reddens: A Mie-Hapke model, *Lunar Planet. Sci. Conf.* **41st**, Abstract 1604.
- Lucey, P. G., and S. K. Noble (2008), Experimental test of a radiative transfer model of the optical effects of space weathering, *Icarus*, **197**, 348–353.
- Lucey, P. G., G. J. Taylor, and E. Malaret (1995), Abundance and distribution of iron on the Moon, *Science*, **268**, 1150–1153, doi:10.1126/science.268.5214.1150.
- Lucey, P. G., D. T. Blewett, and B. R. Hawke (1998), Mapping the FeO and TiO₂ content of the lunar surface with multispectral imaging, *J. Geophys. Res.*, **103**, 3679–3699, doi:10.1029/97JE03019.
- Lucey, P. G., D. T. Blewett, and B. L. Jolliff (2000a), Lunar iron and titanium abundance algorithms based on final processing of Clementine UVVIS data, *J. Geophys. Res.*, **105**, 20,297–20,306, doi:10.1029/1999JE001117.
- Lucey, P. G., D. T. Blewett, G. J. Taylor, and B. R. Hawke (2000b), Imaging of lunar surface maturity, *J. Geophys. Res.*, **105**, 20,377–20,386, doi:10.1029/1999JE001110.
- McCauley, J. F. (1967), Geologic map of the Hevelius region of the Moon, *U.S. Geol. Surv. Misc. Geol. Invest. Map*, I-491.
- McCauley, J. F. (1973), Geologic map of the Grimaldi quadrangle of the Moon, *U.S. Geol. Surv. Misc. Geol. Invest. Map*, I-740.
- Milton, D. J. (1968), Geologic map of the Theophilus Quadrangle of the Moon, *U.S. Geol. Surv. Misc. Geol. Invest. Map*, I-546.
- Mitchell, D. L., J. S. Halekas, R. P. Lin, S. Frey, L. L. Hood, M. H. Acuña, and A. Binder (2008), Global mapping of lunar crustal magnetic fields by Lunar Prospector, *Icarus*, **194**, 401–409, doi:10.1016/j.icarus.2007.10.027.
- Moore, H. J., C. A. Hodges, and D. H. Scott (1974), Multiringed basins illustrated by Orientale and associated features, *Proc. Lunar Sci. Conf.* **5th**, vol. 1, 71–100.
- Murchie, S., et al. (2002), Color variations on Eros from NEAR multispectral imaging, *Icarus*, **155**, 145–168.
- Neish, C. D., D. T. Blewett, D. B. J. Bussey, S. J. Lawrence, M. Mechtley, B. J. Thomson, M. S. Robinson, and the Mini-RF Team (2010), The surficial nature of lunar swirls as revealed by the Mini-RF instrument, *Lunar Grad. Conf.*, Abstract 1806.
- Nicholas, J. B., M. E. Purucker, and T. J. Sabaka (2007), Age spot or youthful marking: Origin of Reiner Gamma, *Geophys. Res. Lett.*, **34**, L02205, doi:10.1029/2006GL027794.
- Noble, S. K., and C. M. Pieters (2003), Space weathering on Mercury: Implications for remote sensing (in Russian), *Astron. Vestnik*, **37**, 34–39, (*Sol. Syst. Res.*, Engl. Transl.), **37**, 31–35.
- Noble, S. K., C. M. Pieters, and L. P. Keller (2007), An experimental approach to understanding the optical effects of space weathering, *Icarus*, **192**, 629–642.
- Norman, M. D., R. A. Duncan, and J. J. Huard (2010), Imbrium provenance for the Apollo 16 Descartes terrain: Argon ages and geochemistry of lunar breccias 67016 and 67455, *Geochim. Cosmochim. Acta*, **74**, 763–783.
- Opanasenko, N., and Y. Shkuratov (2004), The Reiner Gamma formation as characterized by Earth-based photometry at large phase angles, *Lunar Planet. Sci.*, **XXXV**, Abstract 1493.
- Paige, D. A., et al. (2009), The Lunar Reconnaissance Orbiter Diviner Lunar Radiometer Experiment, *Space Sci. Rev.*, **150**, 125–160, doi:10.1007/s11214-009-9529-2.
- Pieters, C. M., E. M. Fischer, O. Rode, and A. Basu (1993), Optical effects of space weathering: The role of the finest fraction, *J. Geophys. Res.*, **98**, 20,817–20,824.
- Pieters, C. M., L. A. Taylor, S. K. Noble, L. P. Keller, B. Hapke, R. V. Morris, C. C. Allen, D. S. McKay, and S. Wentworth (2000), Space weathering on airless bodies: Resolving a mystery with lunar samples, *Meteorit. Planet. Sci.*, **35**, 1101–1107.

- Pinet, P., V. Shevchenko, S. Chevrel, Y. Daydou, and C. Rosemburg (2000), Local and regional lunar regolith characteristics at Reiner Gamma Formation: Optical and spectroscopic properties from Clementine and Earth-based data, *J. Geophys. Res.*, **105**, 9457–9475, doi:10.1029/1999JE001086.
- Pohn, H. A. (1972), Geologic map of the Tycho quadrangle of the Moon, *U.S. Geol. Surv. Misc. Geol. Invest. Map, I-713*.
- Purucker, M. E. (2008), A global model of the internal magnetic field of the Moon based on Lunar Prospector magnetometer observations, *Icarus*, **197**, 19–23, doi:10.1016/j.icarus.2008.03.016.
- Rava, B., and B. Hapke (1987), An analysis of the Mariner 10 color ratio map of Mercury, *Icarus*, **71**, 397–429.
- Richmond, N. C., and L. L. Hood (2008a), A preliminary global map of the vector lunar crustal magnetic field based on Lunar Prospector magnetometer data, *J. Geophys. Res.*, **113**, E02010, doi:10.1029/2007JE002933.
- Richmond, N. C., and L. L. Hood (2008b), Understanding lunar magnetism: Present status and future work using surface magnetometers, *Lunar Planet. Sci.*, **XXXIX**, Abstract 2258.
- Richmond, N. C., L. L. Hood, J. S. Halekas, D. L. Mitchell, R. P. Lin, M. Acuna, and A. B. Binder (2003), Correlation of a strong lunar magnetic anomaly with a high-albedo region of the Descartes mountains, *Geophys. Res. Lett.*, **30**(7), 1395, doi:10.1029/2003GL016938.
- Richmond, N. C., L. L. Hood, D. L. Mitchell, R. P. Lin, M. H. Acuna, and A. B. Binder (2005), Correlations between magnetic anomalies and surface geology antipodal to lunar impact basins, *J. Geophys. Res.*, **110**, E05011, doi:10.1029/2005JE002405.
- Robinson, M. S., and P. G. Lucey (1997), Recalibrated Mariner 10 color mosaics: Implications for Mercurian volcanism, *Science*, **275**, 197–200.
- Russell, C. T., P. J. Coleman Jr., B. K. Fleming, L. Hilburn, G. Ioannidis, B. R. Lichtenstein, and G. Schubert (1975), The fine-scale lunar magnetic field, *Proc. Lunar Sci. Conf. 6th*, 2955–2969.
- Sasaki, S., K. Nakamura, Y. Hamabe, E. Kurahashi, and T. Hiroi (2001), Production of iron nanoparticles by laser irradiation in a simulation of lunar-like space weathering, *Nature*, **410**, 549–554, doi:10.1038/35069004.
- Schultz, P. H. (1976), *Moon Morphology*, 626 pp., Univ. of Texas Press, Austin, Tex.
- Schultz, P. H., and D. E. Gault (1975), Seismic effects from major basin formations on the Moon and Mercury, *Moon*, **12**, 159–177.
- Schultz, P. H., and L. J. Srnka (1980), Cometary collisions with the Moon and Mercury, *Nature*, **284**, 22–26, doi:10.1038/284022a0. (See also Schultz, P. H., and L. J. Srnka (1980) Cometary collisions with the Moon and Mercury (reply), *Nature*, **287**, 86–87, doi:10.1038/287086b0.)
- Scott, D. H., J. F. McCauley, and M. N. West (1977), Geologic map of the west side of the Moon, *U.S. Geol. Surv. Misc. Geol. Invest. Map, I-1034*.
- Shkuratov, Y. G., V. G. Kaydash, and N. V. Opanasenko (1999), Iron and titanium abundance and maturity degree distribution on the lunar near side, *Icarus*, **137**, 222–234.
- Shkuratov, Y., N. Opanasenko, E. Zubko, Y. Grynk, V. Korokhin, C. Pieters, G. Videen, U. Mall, and A. Opanasenko (2007), Multispectral polarimetry as a tool to investigate texture and chemistry of lunar regolith particles, *Icarus*, **187**, 406–416.
- Shkuratov, Y., N. Opanasenko, A. Opanasenko, E. Zubko, S. Bondarenko, V. Kaydash, G. Videen, Y. Velikovsky, and V. Korokhin (2008), Polarimetric mapping of the Moon at a phase angle near the polarization minimum, *Icarus*, **198**, 1–6.
- Shkuratov, Y., V. Kaydash, S. Gerasimenko, N. Opanasenko, Y. Velikovsky, V. Korokhin, G. Videen, and C. Pieters (2010), Probable swirls detected as photometric anomalies in Oceanus Procellarum, *Icarus*, **208**, 20–30.
- Shorthill, R. W. (1973), Infrared atlas charts of the eclipsed Moon, *Moon*, **7**, 22–45.
- Spudis, P. D. (1993), *The Geology of Multi-Ring Impact Basins*, 263 pp., Cambridge Univ. Press, Cambridge, U. K.
- Srivastava, N. (2009), Spectral reflectance studies for maturation trends in a mare and highland swirl, *Lunar Planet. Sci.*, **XL**, Abstract 1577.
- Srnka, L. J., J. L. Hoyt, J. V. S. Harvey, and J. E. McCoy (1979), A study of the Rima Sirsalis magnetic anomaly, *Phys. Earth Planet. Inter.*, **20**, 281–290.
- Staid, M. I., and C. M. Pieters (2000), Integrated spectral analysis of mare soils and craters: Applications to eastern nearside basalts, *Icarus*, **145**, 122–139.
- Starukhina, L., and Y. Shkuratov (2004), Swirls on the Moon and Mercury: Meteoroid swarm encounters as a formation mechanism, *Icarus*, **167**, 136–147.
- Stuart-Alexander, D. E. (1978), Geologic map of the central farside of the Moon, *U.S. Geol. Surv. Misc. Geol. Invest. Map, I-1047*.
- Taylor, L. A., C. M. Pieters, R. V. Morris, L. P. Keller, and D. S. McKay (2001), Lunar mare soils: Space weathering and the major effects of surface correlated nanophase Fe, *J. Geophys. Res.*, **106**, 27,985–28,000, doi:10.1029/2000JE001402.
- Vernazza, P., R. P. Binzel, A. Rossi, M. Fulchignoni, and M. Birlan (2009), Solar wind as the origin of rapid reddening of asteroid surfaces, *Nature*, **458**, 993–995.
- Walker, R. J., and J. J. Papike (1981), The relationship of the lunar regolith <10 μm fraction and agglutinates, part II: Chemical composition of agglutinate glass as a test of the “fusion of the finest fraction” (F3) model, *Proc. Lunar Sci. Conf. 12th*, 421–432.
- Warell, J., and P. G. Valegård (2006), Albedo color distribution on Mercury: A photometric study of the poorly known hemisphere, *Astron. Astrophys.*, **460**, 625–633.
- Whitaker, E. A. (1969), Sublimes, in *Analysis of Apollo 8 Photography and Visual Observations*, SP-201, pp. 34–35, NASA, Washington, D. C.
- Wieczorek, M. A., and B. P. Weiss (2010), Testing the lunar dynamo hypothesis using global magnetic field data, *Lunar Planet. Sci. Conf. 41st*, Abstract 1625.
- Wieczorek, M. A., and M. T. Zuber (2001), A Serenitatis origin for the Imbrium grooves and South Pole-Aitken thorium anomaly, *J. Geophys. Res.*, **106**, 27,853–27,864 doi:10.1029/2000JE001384.
- Wieser, M., S. Barabash, Y. Futaana, M. Holmström, A. Bhardwaj, R. Sridharan, M. B. Dhanya, A. Schaufelberger, P. Wurz, and K. Asamura (2010), First observation of a minimagnetosphere above a lunar magnetic anomaly using energetic neutral atoms, *Geophys. Res. Lett.*, **37**, L05103, doi:10.1029/2009GL041721.
- Wilcox, B. B., P. G. Lucey, and J. J. Gillis (2005), Mapping iron in the lunar mare: An improved approach, *J. Geophys. Res.*, **110**, E11001, doi:10.1029/2005JE002512.
- Wilhelms, D. E. (1987), The geologic history of the Moon, *U.S. Geol. Surv. Prof. Pap.*, **1348**, 302 pp.
- Wilhelms, D. E., and F. El-Baz (1977), Geologic map of the east side of the Moon, *U.S. Geol. Surv. Misc. Geol. Invest. Map, I-948*.
- Wilhelms, D. E., and J. F. McCauley (1971), Geologic map of the nearside of the Moon, *U.S. Geol. Surv. Misc. Invest. Map, I-703*.
- Wilhelms, D. E., K. A. Howard, and H. G. Wilshire (1979), Geologic map of the south side of the Moon, *U.S. Geol. Surv. Misc. Geol. Invest. Map, I-1162*.
- Yamada, M., S. Sasaki, H. Nagahara, A. Fujiwara, S. Hasegawa, H. Yano, T. Hiroi, H. Ohashi, and H. Otake (1999), Simulation of space weathering of planet-forming materials: Nanosecond pulse laser irradiation and proton implantation on olivine and pyroxene samples, *Earth Planets Space*, **51**, 1255–1265.
- Zisk, S. H., H. Masursky, D. J. Milton, G. G. Schaber, R. W. Shorthill, and T. W. Thompson (1972), Apollo 16 landing site: Summary of Earth-based remote sensing data, in *Apollo 16 Preliminary Science Report*, NASA Spec. Publ., SP-315, 29–105–29–110.
- Zisk, S. H., G. H. Pettengill, and G. W. Catuna (1974), High-resolution radar maps of the lunar surface at 3.8 cm wavelength, *Moon*, **10**, 17–50.

D. T. Blewett and E. I. Coman, Johns Hopkins University Applied Physics Laboratory, 11100 Johns Hopkins Road, Laurel, MD 20723, USA. (david.blewett@jhuapl.edu)

J. J. Gillis-Davis and B. R. Hawke, Hawaii Institute of Geophysics and Planetary Sciences, University of Hawaii, 1680 East-West Road, Post 602, Honolulu, HI 96822, USA.

C. G. Hughes, Department of Geology and Planetary Science, University of Pittsburgh, Pittsburgh, PA 15260, USA.

M. E. Purucker, Raytheon at Planetary Geodynamics Laboratory, NASA Goddard Space Flight Center, Greenbelt, MD 20771, USA.